UNIVERSITEIT•STELLENBOSCH•UNIVERSITY
jou kennisvennoot • your knowledge partner

Stochastic inversion of fire test data for the T-dependant thermal diffusivity of SA pine

by

Liza Stewart
21555575

Project (Civil Engineering) 458

2021-02-014

Study leader: Prof N de Koker

November 2021

UNIVERSITEIT•STELLENBOSCH•UNIVERSITY
jou kennisvennoot • your knowledge partner

Plagiaatverklaring / *Plagiarism Declaration*

1. Plagiaat is die oorneem en gebruik van die idees, materiaal en ander intellektuele eiendom van ander persone asof dit jou eie werk is.
   Plagiarism is the use of ideas, material and other intellectual property of another's work and to present is as my own.

2. Ek erken dat die pleeg van plagiaat 'n strafbare oortreding is aangesien dit 'n vorm van diefstal is.
   I agree that plagiarism is a punishable offence because it constitutes theft.

3. Ek verstaan ook dat direkte vertalings plagiaat is.
   I also understand that direct translations are plagiarism.

4. Dienooreenkomstig is alle aanhalings en bydraes vanuit enige bron (ingesluit die internet) volledig verwys (erken). Ek erken dat die woordelikse aanhaal van teks sonder aanhalingstekens (selfs al word die bron volledig erken) plagiaat is.
   Accordingly all quotations and contributions from any source whatsoever (including the internet) have been cited fully. I understand that the reproduction of text without quotation marks (even when the source is cited) is plagiarism

5. Ek verklaar dat die werk in hierdie skryfstuk vervat, behalwe waar anders aangedui, my eie oorspronklike werk is en dat ek dit nie vantevore in die geheel of gedeeltelik ingehandig het vir bepunting in hierdie module/werkstuk of 'n ander module/werkstuk nie.
   I declare that the work contained in this assignment, except where otherwise stated, is my original work and that I have not previously (in its entirety or in part) submitted it for grading in this module/assignment or another module/assignment.

Signature: .....
L. Stewart (21555575)

Datum: .....

Abstract

Stochastic inversion methods such as Markov chain Monte Carlo and optimisation methods were used to determine the thermal diffusivity of SA Pine. Thermal diffusivity can be easily calculated from thermal conductivity, and conductivity can be more directly solved through modelling; the focus was therefore moved to the calculation of thermal conductivity. A finite element model was constructed to model a 100mm element exposed to the ISO 846 Fire curve. The model was compared to data previously obtained by S. van der Westhuyzen; this data was also used as the observed quantity in the formulation of the Bayes' model. Using Bayes inversion, a posteriori probability distribution consisting of a likelihood probability and a prior probability was constructed. The finite element model was essential to the calculation of the likelihood probability. The prior probability was based off the thermal conductivity values from EN 1995:1-2-2004. New thermal conductivity values were estimated through Markov chain Monte Carlo inversion and the Maximum a Posteriori was found though optimisation. The Markov chain Monte Carlo and maximum a posteriori thermal conductivity were not equal, supporting the hypothesis that the distribution is not normal. The model was rerun with the new thermal conductivity estimates and the models were compared to the the measured data. The new estimated conductivity values resulted in more accurate modelling of the temperature in SA Pine when exposed to fire. From the new conductivity estimates combined with known values of density and specific heat capacity, the thermal diffusivity could be successfully calculated.

Uittreksel

Stogastiese inversie metodes soos Markovketting Monte Carlo en optimalisering metodes was gebruik om die termiese diffusiwiteit van Suid-Afrikaanse dennehout te bepaal. Termiese diffusiwiteit kan maklik uitgewerk word as die termiese geleidingsvermoë bekend is. Termiese geleidingsvermoë kan meer direk bepaal word deur modellering, en daarom het die fokus verskuif na die bepaling van die termiese geleidingsvermoë. 'n Eindige element model was saamgestel om a 100mm element wat blootgestel is aan die ISO 846 vuur kurwe te modelleer. Dié model was vergelyk met data wat vooraf deur S. van der Westhuyzen gemeet is; hierdie data was gebruik as die waarneembare hoeveelheid in die opstelling van die Bayes model. Deur gebruik van Bayes inversie was 'n posterior verspreiding wat bestaan uit 'n waarskynlikheid verspreiding en 'n voorafgaande verspreiding bepaal. 'n Eindige element model was benodig om die waarskynlikheid verspreiding uit te werk. Die voorafgaande verspreiding was gebaseer op die termiese geleidingsvermoë waardes in EN 1995:1-2-2004. Nuwe waardes vir die termiese geleidingsvermoë was bepaal deur Markovketting Monte Carlo inversie en die maximum a posteriori was gevind deur optimalisering. Die gemiddeld wat bevind was deur die Markovketting Monte Carlo en deur die maximum a posteriori was nie gelyk nie, wat die hipotese dat die verspreiding nie normaalverspreid is nie ondersteun. Nuwe temperatuur uitslae was met behulp van die model en die nuwe termiese geleidingsvermoë bepaal. Die nuwe termiese geleidingsvermoë waardes het gelei tot meer akkurate modellering van die temperatuur in Suid-Afrikaanse dennehout wat blootgestel is aan vuur. Die termiese diffusiwiteit kon bereken word vanaf die nuwe geleidingsvermoë waardes, die bekende digtheid, en die spesifieke hittekapasiteit.

Acknowledgements

I would like to thank Prof. de Koker for all his support and encouragement, and for believing in me even when I didn't necessarily believe in myself. My loved ones and parents cannot be forgotten for keeping me sane and for providing countless mugs of coffee. I want to thank my friends and classmates for listening to me and for sharing in the frustrations along the way. A special mention goes to Danie Els for creating this lovely LaTeX template, and to all the strangers on StackExchange for helping me master the template.

Let all that I am praise the Lord;
may I never forget the good things He does for me.
Psalms 103:2

Contents

List of Figures

List of Tables

Nomenclature

Variables

κ	Thermal conductivity	$[\,\mathrm{W/(m\ K)}\,]$
α	Thermal diffusivity	$[\,\mathrm{m^2/s}\,]$
c_p	Heat capacity of pine	$[\,\mathrm{J/(kg\ K)}\,]$
c_A	Heat capacity of air	$[\,\mathrm{J/(kg\ K)}\,]$
ρ	Density	$[\,\mathrm{kg/m^3}\,]$

Chapter 1

Introduction

This chapter will introduce the problem that is addressed in this project. Previous similar projects will be investigated, and the value of this research will be presented.

1.1 Background and Motivation

Traditionally, the thermal diffusivity (otherwise referred to as the α-value) of timber is based simply on the EN 1995:1-2-2004(CEN, 2004), further referred to as the Eurocode, or similar standards. This research project will aim to obtain the thermal diffusivity of cross-laminated SA-Pine timber by further analysing data originally obtained by van der Westhuyzen *et al.* (2020) for their study of the samples' charring rate.

The thermal diffusivity of timber is an unobservable quality that cannot be measured directly. However, thermal diffusivity is directly related to thermal conductivity (κ) and can be calculated when thermal conductivity is known. The majority of this report will therefore discuss the methods used to obtain the thermal conductivity or κ-values, and the diffusivity will be calculated when interpreting the results.

Conductivity can be related to measurements of temperature and time through differential models. When heat conduction is calculated using finite element methods, the process is usually simplified to a linear problem (Fish, 2007). Due to changes in thermal conductivity of timber with temperature, as can be seen in EN 1995:1-2-2004 (page 49) and Figure 3.22, the conductivity cannot be linearly modelled. The problem therefore lends itself to being analysed by inversion techniques. This approach will allow us to obtain information about the conductivity based on the combined information assumed prior to measuring (further referred to as the prior) and the measured data. Statistical inversion delivers a probability distribution, thereby providing a collection of conductivity estimates and their corresponding probabilities. The approach

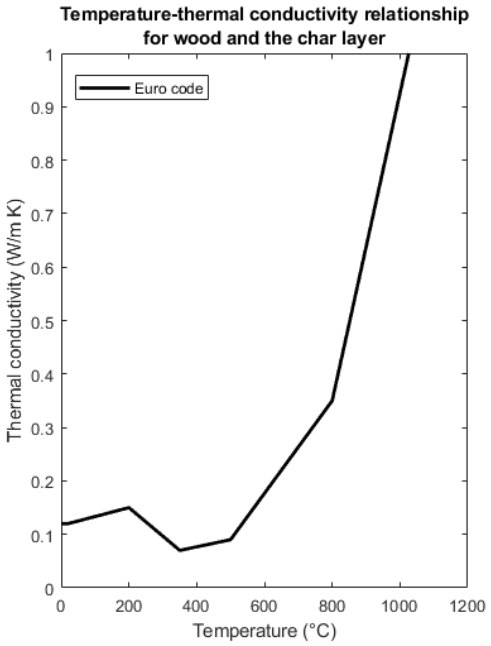

Figure 1.1: Standard temperature-thermal conductivity relationship for timber from (CEN, 2004)

taken in this report is unique due to the nature of the data used, as the main purpose of this data's collection had been to determine char rates and not thermal conductivity or diffusivity. This difference in research goals means that more assumptions had to be made compared to an experiment that intended to determine the thermal conductivity and thus would have controlled those variables.

Currently, the fire rating of specific timber samples is based on fire tests conducted in a furnace. The furnace's temperature is continually increased in accordance with the Standard or ISO 834 fire curve as specified in ISO 834 (ISO, 1999). This process becomes very costly if it must be repeated every time timber is used for construction, as timber has seen increased usage for multiple story construction projects over the past decades. This increase is partially due to the sustainability of timber as a construction material: not only is it renewable but it also has a small carbon footprint (Salvadori, 2017). Obtaining and standardising thermal diffusivity values for different species of timber will assist in more accurate modelling. If modelling accuracy can be increased, the use of modelling to confirm fire tests or to replace small-scale fire tests will become more feasible.

1.2 Aim and objectives

During the course of the project, the student will aim to meet the following objectives:

1. Modify a time-dependant heat transfer finite element model implemented in MATLAB into an accurate and effective function;
2. Compare the model to the measured data;
3. Solve for the thermal diffusivity using Bayesian inversion using the following methods:
   (a) Markov chain Monte Carlo
   (b) Maximum a posteriori

1.3 Literature study

In their article *Simple Method to Determine the Diffusivity of Green Wood*, Frayssinhes *et al.* (2020) determined the global diffusivity of a Douglas fir green log using inverse identification methods. Their experiment involved submerging the log with K-type thermocouples attached at each end in a boiler filled with water at 60°C. The thermocouples were specifically placed to improve the accuracy of the diffusivity ratio calculation. The finite element model constructed for their calculations used linear interpolation with four-node quadrangle elements. An analytical model was also constructed using the heat conduction and diffusion equations. The thermal diffusivity was calculated by minimising the root mean square error between the slope of the measured data and the finite element model. This research intended to assist the peeling industry in making the pretreatment process more cost-effective. The method proved to be effective at determining the thermal diffusivity of green Douglas fir logs, as the κ-values obtained were comparable to those from literature. However, the temperatures at which their experiments were conducted and the final application of their data differ greatly from that of van der Westhuyzen.

Wagner *et al.* wrote an article in March 2021 where Bayesian model inversion was used with stochastic spectral embedding. Spectral embedding, or spectral likelihood expansion, was used to solve for the likelihood function in such a way that sampling is not necessary. Similarly to this report, the research of Wagner *et al.* (2021) involved the creation and use of a Bayesian model to solve a heat diffusion problem. The likelihood function used in their analysis was similar to the likelihood function explained later in this report. The focus of the article was to determine the accuracy of stochastic spectral likelihood

Table 1.1: κ-values at different temperatures obtained by König and Walleij

Temperature °C	Conductivity W/(m K)
0	0.12
200	0.15
350	0.07
500	0.09
800	0.35
1200	1.50

embedding, stochastic spectral embedding and spectral likelihood functions to calculate the thermal diffusivity. A Markov chain Monte Carlo analysis was done to compare to values from other methods. Although the Markov chain Monte Carlo method was not discussed in detail in the article, the usage of Bayesian modelling to create a likelihood function that the MCMC analysis could be done on is similar to the process followed throughout this project.

During the World Conference on Timber Engineering, Thi *et al.* (2016) presented a paper regarding the mathematical modelling of timber in fire. In their model they considered the accounted for heat transfer through thermal conduction, convection and radiation similar to what was done in the model created for this project. Their model was created in Abaqus and compared the model using different thermal conductivities and specific heat values. The main goal of this model was to determine the change of the cross-section of timber due to charring, to achieve this the model had to be constructed in three dimensions. Their research proves that numerical modelling can be used to accurately predict the charring of timber and the change in cross section. The effect of different thermal conductivity values on the resulting temperature curves produced by their model is also clear in their results.

The current Eurocode thermal κ-values were based on a study by König and Walleij (1999). The most significant change in the κ-values obtained by König and Walleij compared to those of previous studies occurred after 350°C. This significant jump in the thermal conductivity is due to the values modelled by the authors also encompassing the additional heat transfer caused by cracks in the charred layer. This cracking effect was assumed to occur at around 500°C. These values were solved for using the computer program TEMPCALC. TEMPCALC is based on a two-dimensional finite element model that solves for the temperature dependant thermal properties using the differential heat transfer equations. The values obtained by König and Walleij are shown in Table 1.1.

Chapter 2

Technical Foundation

In this chapter, detailed explanations of the algorithms and concepts applied throughout the project are presented. This chapter aims to enable the reader to better understand the implementation and reasoning for the use of specific methods.

2.1 Thermal properties of fire exposed timber

Specific thermal properties of timber must be thoroughly understood to allow for accurate modelling and interpretation of the results. After 100°C, the temperature exposure causes the timber structure to break down in such a way that it will not return to the original state after cooling. This breakdown is generally referred to as thermal degradation, which can be broken into four categories (White and Dietenberger, 2001) (Shi and Chew, 2021). These categories are based on the different reactions that occur, and are briefly summarised below and visualised in Figure 2.1:

- Above 100°C and below 200°C, the moisture in the timber is evaporated and other non-combustible gasses are released.
- Between 200°C and 300°C, carbon monoxide is released in significant quantities, and some of the timber components undergo a change in chemical composition due to the high temperatures.
- Temperatures above 300°C and before 450°C are significant due to the amount of flammable volatiles released and the break of carbon linkages at 370°C.
- At temperatures higher than 450°C, the remaining timber is charred and any further degradation is due to oxidation from carbon monoxide, carbon dioxide, and water.

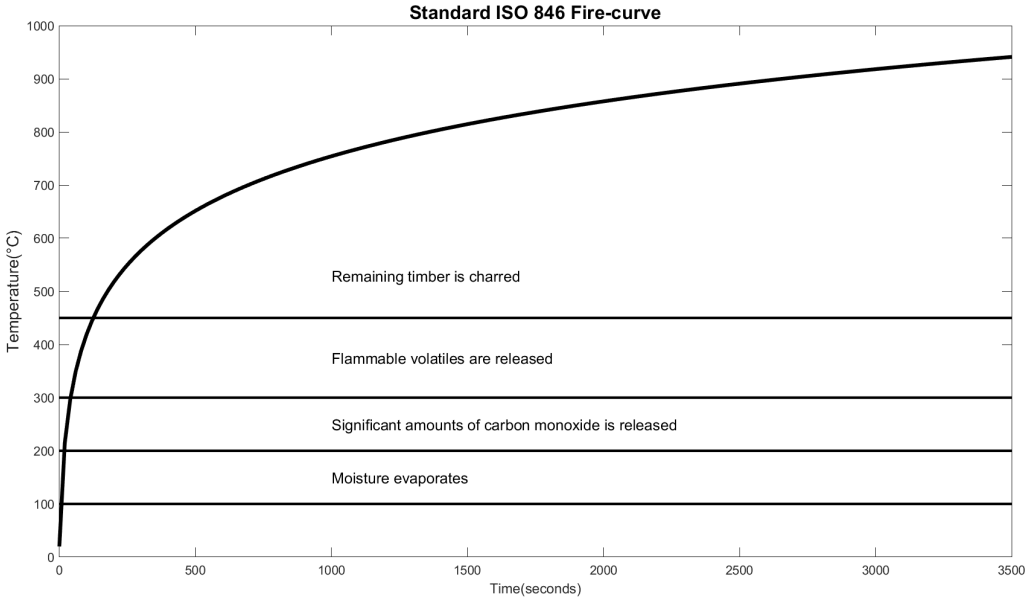

Figure 2.1: Visualisation of thermal degradation categories

Table 2.1: c_p and ρ at different temperatures

Temp (°C)	c_p $(J/(kg\ K))$	ρ (kg/m^3)	$c_p\rho$ $(kJ/(kg\ K))$
0	1530	479	732.8
60	1652	479	791.3
100	13600	479	6514.4
140	2090	408	852.7
200	2000	408	816.0
350	850	220	187.0
500	1200	142	170.4
800	1650	110	181.5
1200	1650	100	165.0

Timber undergoes physical and chemical changes as temperature changes; it therefore makes sense that its thermal properties (such as its specific heat capacity c_p and its density ρ) also varies with temperature. As the thermal conductivity and thermal diffusivity will only be assessed at specific temperatures, the specific heat and density at only those temperatures will be summarised below. All the thermal properties of various timber species at high temperatures were discussed in a research article by Shi and Chew (2021). In their article, they provide a general expression for the thermal conductivity of softwoods (Equation 2.1) and char (Equation 2.2) with all temperatures in

Kelvin.

$$\kappa = 0.124 + 0.8432 \times 10^{-4}(\mathrm{T} - 293) \tag{2.1}$$

$$\kappa = 0.091 + 8.2 \times 10^{-4}\mathrm{T} \tag{2.2}$$

For this project, the temperature of at which charring occurs will be taken as 300 °C following the research of van der Westhuyzen *et al.*. Using the equations of Shi and Chew, the following κ-values in Table 2.2 are obtained. These values provide additional insight into the attempts made to quantify the values of thermal diffusivity for different timbers species. These κ-values are not very close to the Eurocode values and a more linear relationship between conductivity and temperature was assumed than in the Eurocode. The Eurocode κ-values were therefore accepted as more accurate and will be used henceforth.

Table 2.2: κ-values at different temperatures using equations from Shi and Chew (2021)

Temperature °C	Conductivity W/(m K)
0	0.1223
60	0.127
100	0.131
140	0.134
200	0.139
350	0.152
500	0.725
800	0.971
1200	1.299

2.1.1 Heat conduction and diffusion

Heat is transferred within an element if a temperature gradient is present The rate at which heat is transferred is directly influenced by the thermal conductivity of the material. This project focuses on heat transferred via conduction, but heat can also be transferred in the form of thermal radiation or convection Fish (2007). The heat conduction equation or Fourier's Law of heat conduction (Fourier, 1878) can be simply expressed in Equation 2.3. Where heat flux is expressed as a partial differential equation dependant on the temperature and thickness of the element.

$$q = k\frac{\Delta T}{L} \tag{2.3}$$

More information can be added if the temperature only varies in one direction. The thermal conductivity can also be expressed as a negative since heat always flows from warm to cold. Fourier's Law can then be written as in Equation 2.4:

$$q = -k\frac{\partial T}{\partial x} \tag{2.4}$$

Derivation of the heat conduction equation over time leads to the heat diffusivity equation, Equation 2.5:

$$\frac{\partial T}{\partial t} = -\alpha\frac{\partial^2 T}{\partial x^2} \tag{2.5}$$

where

$$\alpha = \frac{\kappa}{c_p \rho} \tag{2.6}$$

As is evident in Equation 2.6, knowing the specific heat capacity and density of the timber at different temperatures is crucial. The values in Table 2.1 will be used in conjunction with the κ-values determined through simulation to calculate new thermal diffusivity values.

2.2 Finite Element Method

The finite element method (or finite element analysis) is used when the behaviour of a large element cannot be accurately depicted by a simple mathematical equation. Modelling the behaviour of large and complex systems is a near impossible task without breaking the problem into smaller understandable parts. The finite element method enables engineers and scientists to break a large problem or element into comprehensible and definable parts (Zienkiewicz and Taylor, 2000). This allows approximations and assumptions to be made at a small scale without affecting the large scale significantly, such as assuming linear behaviour between nodes. It follows that the accuracy of a finite element model is highly dependant on the number of elements used and only improves with more elements. Unfortunately, the computational time needed to analyse a model with a thousand elements is significantly more than needed for a model with fewer elements. The fine balance between sufficient accuracy and short enough computational time should always be kept in mind.

2.2.1 Origin

The finite element method (FEM) used today is the sum of decades of research. In an article by Gupta and Meek (1996), the authors discuss the five main contributors to the finite element method. They report that the idea behind the finite element method was initially explored in the 1943 article by

Courant. Courant acknowledges the complex nature of mathematical problems in his first paragraph by stating: "Mathematics is an indivisible organism uniting theoretical contemplation and active application." He goes on to discuss the variational method created by Lord Rayleigh and Walther Ritz and the shortcomings of their methods. He concludes that using few elements does not provide accurate local estimations, but instead the interpolation will provide approximations of the actual quantities that are sufficient for engineering problems. As his paper did not go into depth into the calculations, Courant cannot be accredited with the full development but rather with the starting point. Gupta and Meek (1996) further points out that in 1954, J. Argyris published an article where the details of his calculations are clear and matrix formulation can be seen. The finite element method as known today were directly defined and clarified in a textbook by Zienkiewicz in 1957. This textbook is now in its fifth edition of print and has been continuously updated and was used for this project.

2.2.2 Boundary constraints

An important part of finite element models is the method by which the known information is embedded into the model. The main method is by defining boundary conditions at known points. The two types of boundary conditions used in this project are Dirichlet boundaries and Newmann boundaries.

Named after Johann P.G.L Dirichlet (Cheng and Cheng, 2005), Dirichlet boundaries force the solution function to be equal to the prescribed value at the boundary. Newmann boundaries prescribe that the derivative of the solution function be equal to the predetermined value. In the context of this problem, the Dirichlet boundaries prescribe the temperatures at the boundaries and the Newmann boundaries prescribe the heat flux at the boundaries.

2.3 Bayes' theorem of inverse problems

The method of statistical inversion is dependant on a fundamental understanding of the Bayes' theorem of inverse problems. This understanding was obtained through studying Chapter 3 of *Statistical and Computational Inverse Problems* by Kaipio and Somersalo (2005). There are four principles of statistical inversion that are essential to the thorough understanding of these models.

Firstly is the principle that any variable in the model needs to be modelled as a random variable. This randomness must be based on the extent of information that is available. To ensure that the extent of knowledge is accurately portrayed in the model, the extent of knowledge will be coded into the probability distributions assigned to the different variables. Finally, it needs to be

understood that the solution of a statistical inversion is a posterior probability distribution. A generalised equation of Bayes' theorem can be seen in 2.7 taken from Kaipio and Somersalo (2005).

$$\pi^*(x) = \pi(x|y_{\text{observed}}) = \frac{\pi_{\text{pr}}(x)\pi(y_{\text{observed}}|x)}{\pi(y_{\text{observed}})} \tag{2.7}$$

Further application of Bayes' theorem of inverse problems to the project at hand is discussed in Section 3.3

2.4 Markov chain Monte Carlo

Markov chain Monte Carlo (MCMC) is a method of integration that will be used to determine the mean of the κ-values at specific temperatures. Markov chain Monte Carlo is a method that was created by combining the concept of Monte Carlo sampling and a Markov chain. To fully understand MCMC, its underlying methods must be investigated further. For a better understanding of this concept, *Introducing Markov chain Monte Carlo* by Gilks *et al.* (1996), Kaipio and Somersalo (2005), and various websites Brownlee (2019), Wiecki (2015) were consulted.

2.4.1 Markov chains

The core principle of a Markov chain is that the next value (x_{n+1}) in a sequence is dependent on the current value (x_n). A step size that indicates the range within the next point falls in. Values are then randomly generated but restricted to be within this range. This concept can be visualised as follows: the accepted point (x_1) is in the centre of a square. The next possible random point is randomly generated but still within the square (our search range). After this next number is selected, the square moves such that the new point (x_2) is now the centre, and so it continues. See Figure 2.2 for clarification. The above example simplifies the concept, but this understanding can now be expanded. If every coordinate direction in the aforementioned simple example is seen as a single entry in the $\mathbf{x}$ vector, then the example has two independent values. More or fewer values can be used depending on the problem. Another level of complication can be added if it is taken into account that every point in the square is no longer equally likely. A distribution within the square can be chosen, for example simply a normal distribution. The shape of the square then warps into a stranger shape with points closer to the center being more likely choices and the edges being less likely.

The purpose of a Markov chain is for the chain to converge to a distribution and be independent on the very initial estimation. In principle, it should then reach a near stationary distribution. Since Markov chains are not used if we

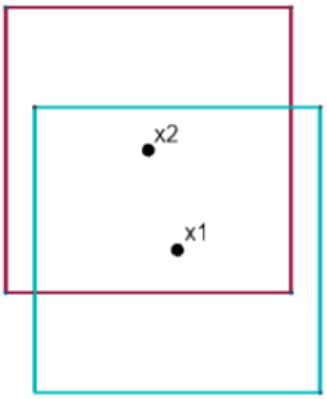

Figure 2.2: Two-dimensional example of Markov chain application

know the answer, a way to determine when values are no longer affected by the initial estimate is needed (Gilks *et al.*, 1996). The simple proposed solution is the concept of burn-in. The concept of conventional burn-in for usage in Markov chains are disputed as the Markov chain itself is created in such a way that values are only directly dependant on the value immediately before them (Meyn and Tweedie, 1993). Burn-in in the Markov chain sense can simply be referred to as the removal of the initial samples of low probability to increase the accuracy of the average taken after all the iterations (Cook, 2016).

2.4.2 Monte Carlo Integration

Monte Carlo integration is used to evaluate a probability distribution that cannot be solved simply. The evaluation is done by drawing a collection of random values from the distribution. These values are then used as the sample, and a sample mean is taken. The arithmetic sample mean can be used to approximate the population mean per the law of large numbers (Gilks *et al.*, 1996).

2.4.3 Metropolis-Hastings Algorithm

The Metropolis-Hastings algorithm is one of the available simulation methods based on the MCMC principles. For this project, the Metropolis-Hastings algorithm was chosen above the Gibbs-sampler as the Gibbs sampler can be relatively slow (Murphy, 2012).

All of the random samples generated by the Monte Carlo integration can not be immediately accepted. Here, the acceptance criterion comes into play.

There are multiple options for how a posterior is deemed acceptable; these are elaborated on in the book *Monte Carlo Statistical Methods* by Robert and Casella. The most general acceptance criterion is set out in Equation 2.8 and comes from Kaipio and Somersalo (2005) where the acceptance ratio is compared to 1 and subsequently to a random value generated between 0 and 1.

$$\begin{aligned} &\text{if} \quad \frac{\pi^*(x_2)}{\pi^*(x_1)} > 1 \quad \text{Accept } x_2 \text{ automatically} \\ &\text{or} \quad \frac{\pi^*(x_2)}{\pi^*(x_1)} > \text{rand} \quad \text{Accept } x_2 \\ &\text{else reject and sample new } x_2 \end{aligned} \tag{2.8}$$

Following the acceptance criterion in Equation 2.8, any x_2 with a higher posterior probability than that of the previously accepted value x_1 can be immediately accepted. If this is not the case, the acceptance ratio needs to be compared to a random value. To ensure that more values are accepted at the peak of the distribution, any uphill steps are immediately accepted. Since the distribution is unknown there is a chance of only exploring a local maximum if all downhill values are automatically rejected. This approach allows some downhill movement but still gives preference to uphill movement. This allows full exploration of the distribution with more accepted samples at the peaks.

2.5 Maximum a Posteriori

To ensure a thorough investigation of the thermal diffusivity of timber, the posteriori function will also be optimised to obtain the value with the highest probability (i.e. maximum a posteriori) in addition to the mean. As the implementation will be done using built-in optimisation functions in MATLAB, the technical aspects will briefly explain how that function works. The function used is `fminsearch.m`. In the name of the function, it can be seen that the function will be minimised. This seems counter-intuitive since the intention is to find the maximum of the function. Luckily the minimum is simply a negative maximum.

According to the `fminsearch` MATLAB (2021), the algorithm is based on the Nelder-Mead algorithm (Lagarias *et al.*, 1998). The Nelder-Mead algorithm is an unconstrained heuristic direct search method. The heuristic aspect of the algorithm means that it searches the function space in a guided random manner. For further understanding of the Nelder-Mead optimisation algorithm, Joglekar (2016) was consulted.

Nelder-Mead uses a simplex, a triangle in the dimension needed, to find the minimum. In two dimensions, the simplex is simply a triangle, where each

point has a x and y coordinate and is notated as. A starting value needs to be provided to the algorithm; this will then be one of the points in the first simplex. All the points on the simplex are ordered from best to worst, where the smallest value $f(x)$ is best if minimising. In the two-dimensional example, the centroid of the two best points (x_l, x_s) is calculate. From there, using the value of the function at the simplexes and the centroid, transformations can be performed to find even smaller values. The transformations are applied to change the worst point (x_h) until it is no longer the worst.

The transformations are performed in a specific order. The first transformation is reflection. Point x_h is mirrored around the line that passes through the centroid and x_l and x_s to create x_r. The idea behind this is that the values are lower in that direction so the algorithm attempts to take the biggest stride possible to a lower value. If x_r is better than x_r, the triangle is expanded and x_e is even further in the assumed minimising direction. If x_r is not better than x_h, the reflected point is rejected and the original x_3 is contracted closer to x_1 and x_2. This contracted point (x_c) should ideally have a smaller value than x_h, otherwise a shrink contraction must be performed. In a shrink contraction, x_h and x_s are redefined and pulled closer to x_l with hopes of finding the minimum near the best point.

The result is a simplex that moves over a surface in search of the lowest point, and as it reaches that point, it shrinks until all the points are practically at the same place. When this happens, or the points are close enough to each other as defined when initialising the code, the algorithm stops. Below in Figure 2.3, the different transformations can be seen.

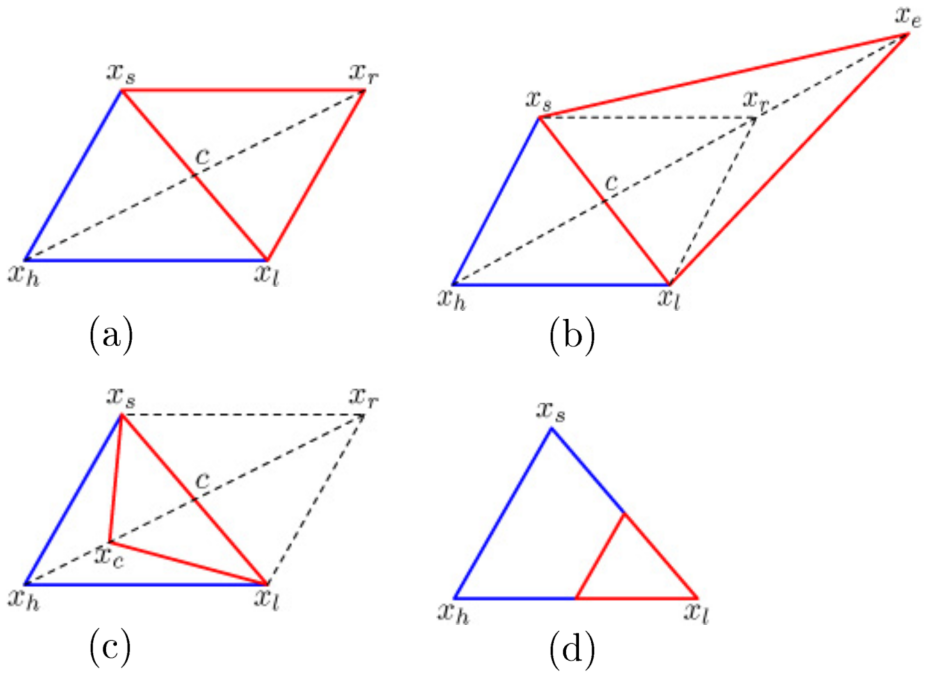

Figure 2.3: Visual representation of Nedler-Mead transformations a) Reflection, b) Expansion, c) Contraction, d) Shrink contraction (Joglekar, 2016)

Chapter 3

Implementation

This chapter will elaborate on the test data used as well as the process that was followed to achieve the results in Chapter 4.

3.1 Existing data

The data used was acquired by van der Westhuyzen *et al.* (2020) for an article assessing the charring rate of both SA-Pine and Eucalyptus. For the purpose of this project, only the data obtained from the SA-Pine test was considered and analysed.

3.1.1 Summary of test

The test was conducted on a sample panel of 100 mm by 0.9 m ×0.9 m cross-laminated SA-pine. This sample was then divided into nine cubes of 100 mm ×100 mm ×100 mm. Each cube was fitted with seven Type K-thermocouples placed at consecutive 16.5 mm drilled holes, as can be seen in Figure 3.1. The test panel was tested in a furnace and was exposed to the standard ISO 834 Fire curve (Figure 3.2 and Equation3.1) on one side and room temperature on the other. The panel was exposed to the fire curve for 50 minutes, at which stage near complete de-lamination was observed and the test was concluded.

$$T = 20 + 345 \log_{10}(8t_{min} + 1) \tag{3.1}$$

In Figure 3.3 the measured temperatures at different depths in the sample can be seen. These same depths will be used in the model and throughout the project to analyse the accuracy of the modelling that was done.

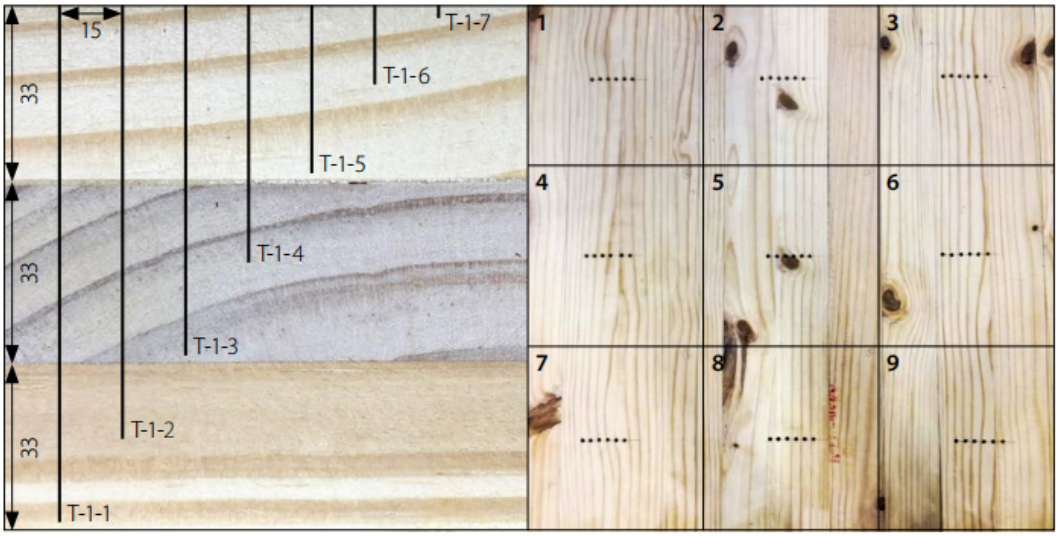

Figure 3.1: Thermocouple layout in test conducted by van der Westhuyzen *et al.* (2020) cross-section (left) and overall layout (right)

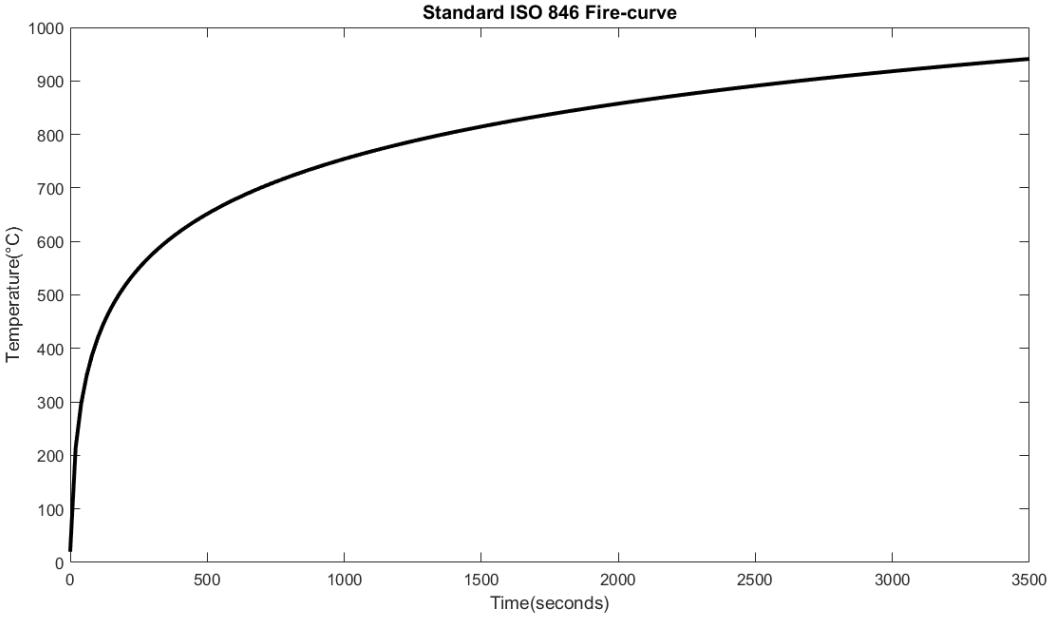

Figure 3.2: Standard ISO fire curve

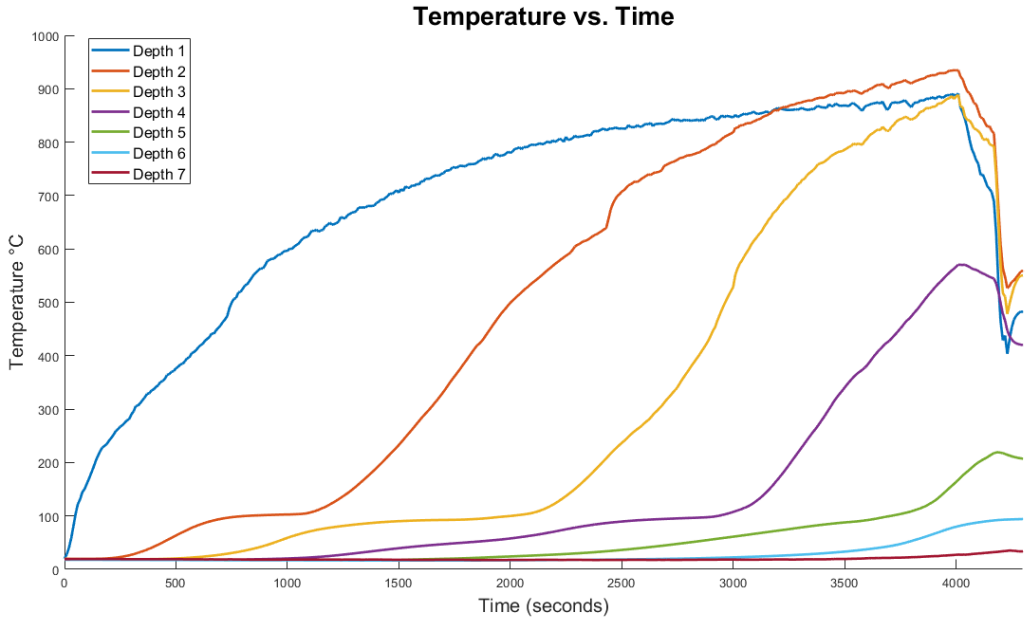

Figure 3.3: Average of measured temperatures at the different depths

3.1.2 Potential inaccuracies

As with most tests, everything is not always perfect. The potential inaccuracies are discussed below. In the data, it was observed that two of the thermocouples malfunctioned during testing and could not be considered This malfunction required that two of the depth measurements were no longer the average between nine samples but instead the average between eight. Another inaccuracy that could potentially influence the accuracy of the final result is the accuracy of the depth of the holes in which the thermocouples were placed.

There is also debate about the significance of the contribution of the timber burning to the temperature inside the furnace. For the purposes of this project, it will be assumed that the timber burning does not contribute to the temperature inside the furnace.

3.2 Finite Element Modelling

A one-dimensional finite element model that simulates what we expect to obtain from the fire tests based on the simplified κ-values provided in EN 1995:1-2-2004 (CEN, 2004) is modified into a function. This function should provide the temperature of the modelled element based on a specified location and thermal conductivity. The derivation and adaptation of the model are expanded on below.

3.2.1 Existing Model

For this project, an existing finite element model of time-dependant conductive heat transfer implemented in MATLAB by Prof. N de Koker was modified for usage in the Bayes' theorem shown in Equation 2.7. This model is used to determine the likelihood function. The current model uses the κ-values as well as the specific heat specified in EN 1995:1-2-2004. The model discretises the wooden element into 32 first-order one-dimensional elements. This number of elements was sufficient to obtain converged results. The model is a one-dimensional finite element model that takes time differentiation into account.

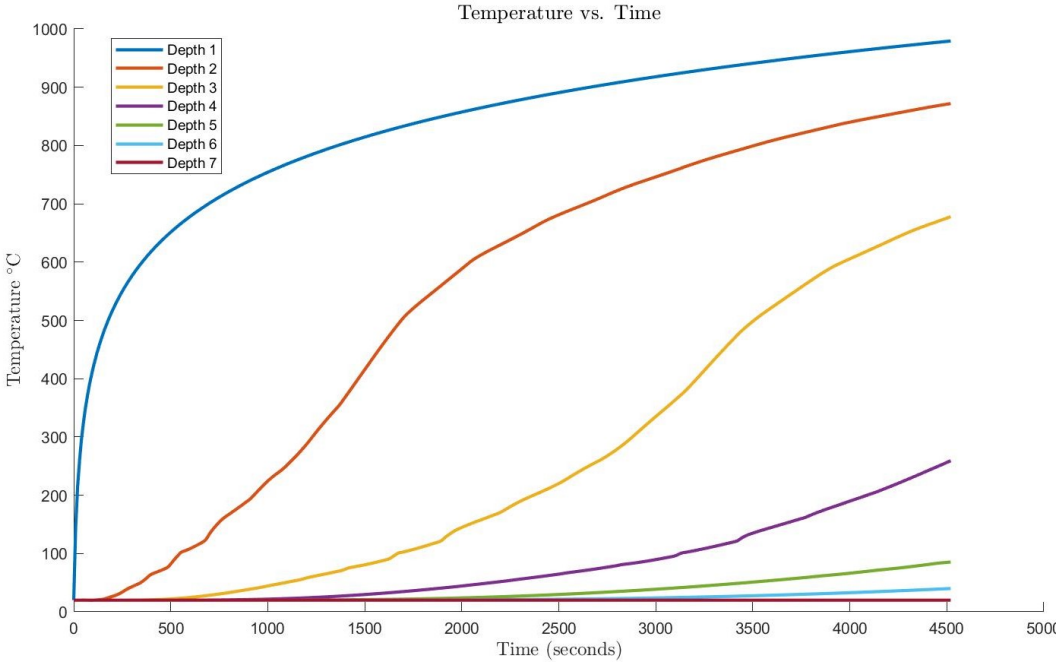

Figure 3.4: Output of finite element model using κ-values as indicated in EN 1995:1-2-2004

3.2.2 Derivation

The following assumptions were made to simplify the model:

1. The air on the side of fire follows the temperature of the fire curve;
2. The air on the cold side remains at 20°C;
3. The timber sample stays intact; and
4. Thermal behaviour is isotropic throughout the model.

Stationary heat conduction

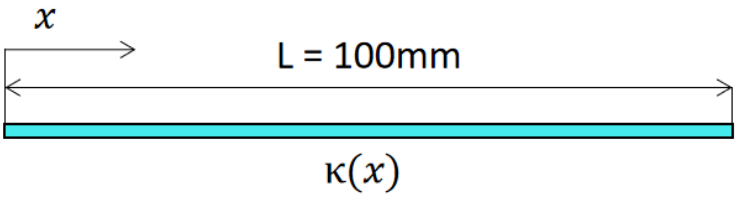

Figure 3.5: Visualisation of model in one-dimension

Based on Hughes (1987) and class notes from Informatics 314, the derivation started as a one-dimensional stationary heat conduction problem with the energy balance equation and the heat conduction equation.

$$q_{,x} - f = 0 \ ...(1) \qquad q = -\kappa u_{,x} \ ...(2) \tag{3.2}$$

Integrating Equation 3.2 (1) over the length of the element (shown in Figure 3.5) and introducing a weighting function $w(x)$ we obtain Equation 3.3, since the derivative of $w(0)$ is known and $q_{,x}$ is unknown. The first term in Equation 3.3 is integrated by parts. After the integration by parts and substituting q with Equation 3.2 (2), Equation 3.4 is produced.

$$\int_{x=0}^{L} w q_{,x} dx - \int_{x=0}^{L} w f dx = 0 \tag{3.3}$$

$$\int_{x=0}^{L} w k u_{,x} dx + \int_{x=0}^{L} w f dx - wq|_0^L = 0 \tag{3.4}$$

In Equation 3.4 the u and w need to be defined. Assuming $u \approx u^h$ and $w \approx w^h$ and using the basis function (N^A), Equation 3.5 is obtained.

$$\begin{aligned} u_e^h &= \sum_B N^B d^B \quad ; \quad w_e^h = \sum_A N^A c^A \\ u_{e,x}^h &= \sum_B N_{,x}^B d^B \quad ; \quad w_{e,x}^h = \sum_A N_{,x}^A c^A \end{aligned} \tag{3.5}$$

Substituting the u and w functions back, we obtain the Galerkin weak form shown in Equation 3.6. In Equation 3.6 the $A \in A_N$ refers specifically to the nodes that have Newmann boundaries, explained in Section 2.2. The variables c^A and d^B are independent of x and can therefore be taken out of the integral. The sum over A and B are also taken out of the integral. After the summing is applied, a matrix of all the possible combinations between A and B can be used to replace the sum. The resulting matrices are shown in Equation 3.7.

When written in matrix form the summing is implied, if matrix form is not written then the expression referrers to the terms that will still be summed.

$$\begin{aligned} \sum_e \int_{\Omega_e} w^h_{e,x} k u^h_{e,x} dx + \sum_e \int_{\Omega_e} w^h_e f dx - w(L) q_L + w(0) q_0 &= 0 \\ \int_{\Omega_e} \sum_A \sum_B N^A_{,x} c^A k N^B_{,x} d^B dx + \int_{\Omega_e} \sum_A N^A c^A f dx - \sum_{A \in A_N} c^A q^A &= 0 \end{aligned} \tag{3.6}$$

$$\mathbf{c}_e^T \mathbf{K}_e^{AB} \mathbf{d}_e + \mathbf{c}_e^T \mathbf{F}_e^f - \mathbf{c}_e^T \mathbf{F}_e^q \tag{3.7}$$

where

$$\mathbf{K}_e^{AB} = \int_{\Omega_e} N^A_{,x} N^B_{,x} k dx$$

$$\mathbf{F}_e^{Af} = \int_{\Omega_e} N^A_{,x} f dx$$

$$\mathbf{F}_e^{Aq} = \begin{cases} q(x_N) & \text{for } x \in \Gamma_N \\ 0 & \text{for other} \end{cases}$$

Boundaries

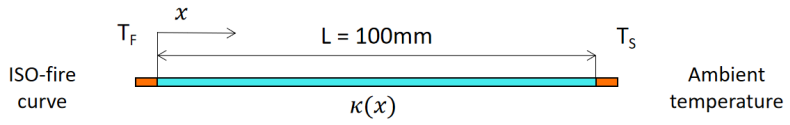

Figure 3.6: Visualisation of one-dimensional model with air elements and external conditions added

One of the additional difficulties in modelling is that the known boundary temperatures are measured in the air of the furnace and assumed for the air outside the furnace. Initially, a long model of air elements was created. These elements are then overlaid with the timber elements to effectively add an air element at each end of the timber model as depicted in Figure 3.6. In the air elements, both heat convection and heat radiation must be taken into account. The equations for heat convection and radiation can be seen in Equations 3.8 and 3.9.

$$\begin{aligned} q_{\text{adv}} &= \nu \rho_A c_A \Delta T = h \Delta T \\ \text{with} \quad \nu &= \text{velocity [m/s]}, \\ \rho_A &= \text{density of air, and} \\ c_\rho &= \text{heat capacity of air} \end{aligned} \tag{3.8}$$

$$\begin{aligned} q_{\text{rad}} &= \varepsilon \sigma \phi \left(T_f^4 - T_S^4 \right) \\ \text{with} \quad \varepsilon &= \text{emissivity}, \\ \sigma &= \text{Stefan-Boltzmann constant} \\ &= 5.670 \times 10^{-8}\ W/(m^2 K^4), \text{ and} \\ \phi &= \text{view factor} = 1 \end{aligned} \tag{3.9}$$

Given that T_S and T_F are known as new equivalent heat flux value can be calculated as in Equation 3.10.

$$q_{\text{con}}^{\text{equiv}} = \kappa^{\text{equiv}} \frac{\Delta T}{\Delta L} = q_{\text{rad}} + q_{\text{adv}} \tag{3.10}$$

Due to the clear relationship between heat flux and thermal diffusivity, the equivalent diffusivity (κ^{equiv}) can be calculated as shown in Equation 3.11.

$$\begin{aligned} \kappa^{\text{equiv}} &= \frac{[q_{\text{rad}} + q_{\text{adv}}]}{\Delta T} \\ &= \frac{\epsilon \sigma \phi \Delta \left(T^4 \right)}{\Delta T / \Delta L} + h \Delta L \\ &= \frac{\epsilon \sigma \Delta \left(T^4 \right)}{\Delta T} + h \end{aligned} \tag{3.11}$$

One-dimensional diffusion

The concept of heat diffusion is thoroughly explained in Section 2.1.1. Below, the mathematical application is explained and steps that were taken to obtain the final model is shown.

$$q_{,x} - f = \frac{\partial Q}{\partial t} = c_p \rho \frac{\partial u}{\partial t} \quad ...(1) \qquad q = -\kappa \frac{\partial u}{\partial x} \quad ...(2) \tag{3.12}$$

Substituting Equation 3.12(2) into Equation 3.12 and taking the derivative as indicated ($q_{,x}$) gives Equation 3.13. As previously discussed, heat conduction (α) is heat diffusion (κ) divided by specific heat (c_p) and density (ρ).

$$\begin{aligned} \therefore -\kappa\frac{\partial^2 u}{\partial x^2} - f = c_p\rho\frac{\partial u}{\partial t} \rightarrow f = 0: \\ \frac{\partial^2 u}{\partial x^2} = -\frac{c_p\rho}{\kappa}\frac{\partial u}{\partial t} \\ \text{or} \\ \frac{\partial u}{\partial t} = -\alpha\frac{\partial^2 u}{\partial x^2} \end{aligned} \tag{3.13}$$

Let $c_p\rho = \lambda$

$$\therefore -\kappa u_{,xx} - \lambda u_{,t} = f \tag{3.14}$$

Then:

$$\int_0^L wq_{,x}\mathrm{d}x - \int_0^L w\lambda u_{,t}\mathrm{d}x - \int_0^L wf\mathrm{d}x = 0 \tag{3.15}$$

Similar to what was done in Equation 3.5 a special approximation is made to obtain Equation 3.16.

$$u \approx u^h \rightarrow u_e^h = \sum_A N^A d^A \quad ; \quad w_e^h = \sum_A N^A L^A \tag{3.16}$$

From the above equations, the below matrix formulation could be assembled where solving for $\mathbf{d}$ and $\dot{\mathbf{d}}$ is the main goal.

$$\mathbf{c}^T\boldsymbol{\kappa}\mathbf{d} + \mathbf{c}^T\mathbf{M}\dot{\mathbf{d}} = \mathbf{c}^T\mathbf{F} \tag{3.17}$$

The vectors $\mathbf{d}$ and $\dot{\mathbf{d}}$ can be obtained by setting $\mathbf{d}_1$ and $\dot{\mathbf{d}}_1$ equal to the initial boundary conditions, setting $\mathbf{v}_1 = 0$, and integrating over time according to v-form time integration in Chapter 8 in *The Finite Element Method* by Hughes shown in detail in Appendix B.

Finally by combining the boundary conditions, stationary heat conduction, and the one-dimensional heat diffusion models, the below formulation in Equation 3.18 is obtained.

$$\mathbf{K}\cdot\mathbf{d} + \mathbf{M}\cdot\dot{\mathbf{d}} = \mathbf{F}' - \mathbf{F}^{Ke} - \mathbf{F}^{Me} = \mathbf{F} \tag{3.18}$$

This can be solved as shown below in Equation 3.19.

$$\begin{aligned} \tilde{\mathbf{d}}_{n+1} &= \mathbf{d}_n + (1-\alpha)\Delta t\mathbf{v}_n \\ (\mathbf{M} + \alpha\Delta t\mathbf{K})\mathbf{v}_{n+1} &= \mathbf{F}_{n+1} - \mathbf{K}\tilde{\mathbf{d}}_{n+1} \\ \rightarrow \mathbf{v}_{n+1} &= (\mathbf{M} + \alpha\Delta t\mathbf{K})^{-1}(\mathbf{F}_{n+1} - \mathbf{K}\tilde{\mathbf{d}}_{n+1}) \\ \rightarrow \mathbf{d}_{n+1} &= \tilde{\mathbf{d}}_{n+1} + \alpha\Delta t\mathbf{v}_{n+1} \\ \mathbf{v} &= \dot{\mathbf{d}} \end{aligned} \tag{3.19}$$

All of these derivations were the basis on which the existing model was built. Understanding this model was essential in ensuring that the adaptation was done correctly.

3.2.3 Adapted Model

The model was changed into a function that takes κ-values and provides a new temperature distribution over the elements for the different κ-values. The code for the adapted model function, `model_kinput.m` can be seen in Appendix A.

The focus of the adaptation was the `main.m` script in the original program. Within the `main.m` function, all of the global variables used were initially defined. The variable definitions were moved into a new function that defines all the global variables used within the original `main.m`, as well as the measured temperature data. Here, the thickness of the timber element was defined as 99 mm and was divided into 30 elements with 2 nodes per element. Two additional elements were also added to incorporate the air elements as explained in Section 3.2.2. The global variable `kpine` was left uninstantiated; instead, it will be fed to the new adapted model (`model_kinput.m`). The timesteps of the model was also set to 10 seconds to coincide with the time-steps in the measurements. Importantly, the `instantiate_all.m` function was called only once and outside of `model_kinput.m`. This was done to ensure that the model remains the same size throughout. Inside `model_kinput.m`, the global `kpine` variable was set equal to the `kinput` variable fed into the model. This adaptation allowed the model to be called within the posterior distribution calculation with different κ-values each time.

3.3 Inversion method

The basis of the stochastic analysis is the adapted Bayesian equation in Equation 3.20 below. Each aspect of this equation will be further explored in the sections below.

$$\pi^*(\mathbf{x}|T) \propto \exp\left(-\frac{(\boldsymbol{\mu}-\mathbf{x})^2}{2\sigma_\mu^2}\right) \cdot \exp\left(-\frac{(\mathbf{T}-\mathcal{M}(\mathbf{x}))^2}{2\sigma_{\text{temp}}^2}\right) \tag{3.20}$$

3.3.1 Prior probability

$$\pi(\mathbf{x}) \propto \exp\left(-\frac{(\boldsymbol{\mu}-\mathbf{x})^2}{2\sigma_\mu^2}\right) \tag{3.21}$$

The prior probability function (Equation 3.21) is based on the κ-values assumed prior to any simulation or analysis. The σ_μ in this equation was assumed to be equal to 0.13 W/(m K). In this case, the prior values are

indicated as μ and refer to the vector of κ-values (Equation 3.22) at specific temperatures as indicated. The temperatures are not exactly similar to the temperatures used in Eurocode; this is due to an attempt at modelling the effect of evaporation at 100 °C.

$$\boldsymbol{\mu} = \begin{bmatrix} 0.12 \\ 0.12 \\ 0.12 \\ 0.12 \\ 0.15 \\ 0.07 \\ 0.09 \\ 0.35 \\ 1.5 \end{bmatrix} \begin{matrix} 0\ ^\circ\mathrm{C} \\ 60\ ^\circ\mathrm{C} \\ 100\ ^\circ\mathrm{C} \\ 140\ ^\circ\mathrm{C} \\ 200\ ^\circ\mathrm{C} \\ 350\ ^\circ\mathrm{C} \\ 500\ ^\circ\mathrm{C} \\ 800\ ^\circ\mathrm{C} \\ 1200\ ^\circ\mathrm{C} \end{matrix} \tag{3.22}$$

The $\mathbf{x}$ (in Equation 3.21) refers to a vector of randomised κ-values that correspond with the same temperatures as the values in the $\boldsymbol{\mu}$ vector. The first iteration of randomised κ-values are generated by creating a random perturbation of the $\boldsymbol{\mu}$ vector. By multiplying the $\boldsymbol{\mu}$ vector with $1.5 \times (0.5 + \mathrm{rand})$, the first values of $\mathbf{x}$ are guaranteed to be within an acceptable range of the prior values. The process of obtaining the $\mathbf{x}$ vector after the first iteration is discussed later in Section 3.3.3.

Initially, the program was written to generate completely random new values for the first iteration of $\mathbf{x}$. This later proved to not only be unnecessary, but also made the process less accurate, as there was a larger burn-in period before the values were anywhere near the actual solution. To increase the accuracy and reduce the number of times the program needed to run to produce a sufficient number of accurate samples, the program was changed to the current method. The prior function in this case was relatively easy to generate and incorporate into the program as a well-defined list of prior values exists.

3.3.2 Likelihood probability function

$$\pi(\mathbf{T}|\mathbf{x}) \propto \exp\left(-\frac{(\mathbf{T} - \mathcal{M}(\mathbf{x}))^2}{2\sigma_{\text{temp}}^2}\right) \tag{3.23}$$

The likelihood probability was more complex to implement, as this required utilisation of the function created from the finite element model as discussed in Section 3.2. This function will output the probability of the modelled values $\mathcal{M}(\mathbf{x})$ given the measured temperature values ($\mathbf{T}$). As can be seen in Equation 3.23, the $\mathcal{M}(\mathbf{x})$ vector is written as a function. The function indicated here takes the new randomised $\mathbf{x}$-vector and then runs the model to provide a new temperature distribution over time at various nodes. The output of

the finite element model was reduced such that only the nodes at the same depths as the thermocouples are provided to the likelihood function. For the likelihood function, the σ_{temp} value was assumed to be 15°C.

3.3.3 Markov chain Monte-Carlo integration

The two main parts of the MCMC integration (as mentioned in Section 2) are: how a value is deemed acceptable (Monte Carlo), and how the next random sample is selected after a previous sample is accepted (Markov chain). As explained in Section 2.4.1, the step size is a crucial part of determining the next random sample. For this project, a step size of 0.05 W/(m K) was chosen.

Compared to the example shown in Figure 2.2, the actual problem is quite more complex. For this project, a log-normal distribution was chosen instead of a uniform distribution. If every coordinate direction in the aforementioned simple example is seen as a single entry in the $\mathbf{x}$ vector, then the example has three κ-values. The problem also technically becomes nine-dimensional, as there are nine separate independent κ-values that must be chained. An important part of the `takesteps.m` function (Appendix A) was to ensure the steps are only taken in a logical direction and that they would not move into an illogical or improbable range. Negatives were specifically forbidden, as a negative thermal diffusivity would mean that heat flows in a direction opposite to the thermal gradient. Provision was made in the function to prevent the algorithm to run away from what we know to be the general area.

The acceptance criterion of the new $\mathbf{x}$-vector is based on the proximity of the new posterior value to the reference posterior value and the previous posterior. A potential problem encountered with the standard acceptance probability method (shown in Section 2.4.2) is that the magnitudes of the values were not considered. This problem lead to many false positives, as incorrect values were accepted even though they were not acceptable. The acceptance criterion was based on Equation 3.24. The δ value was arbitrarily chosen to be 0.02, and initially $\delta = 0.5$ but as can be seen in Figure 3.7 this acceptance was still too lenient. Using $\delta = 0.02$ decreased the acceptance rate of values that were far below one.

$$\exp\left(\frac{\pi^*(\mathbf{x_{n+1}}) - \pi^*(\mathbf{x_n})}{\pi^*(\mathbf{x}_{\text{ref}})\delta}\right) \text{ with } \delta = 0.02 \tag{3.24}$$

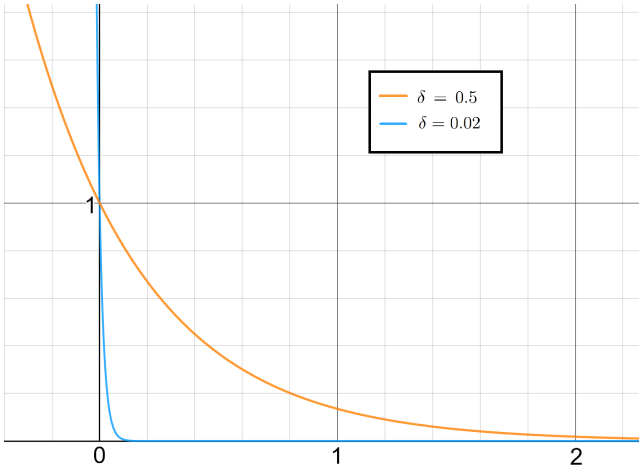

Figure 3.7: Graph explaining the difference in acceptance rates

To allow for sufficient number of samples, the program was run until 20 000 samples were generated. The program was run four times with 5 000 iterations and different starting values each time. Due to computational limitations, more iterations could not be run. Due to burn-in, as explained in Section 2.4.1, the first 100 samples of each run was removed from analysis. This resulted in 19 600 acceptable and useful samples that were analysed.

3.4 MAP parameter estimation

The maximum a posteriori of the posteriori function was also determined to allow for further comparison of results. All the values and constants except for the κ-values were kept the same as in the MCMC integration to allow the results to be compared on the same basis. The optimisation to determine the maximum value of the posteriori function was initially done utilising the built-in MATLAB optimisation algorithm `femsearchmin.m`. The function, `femsearchmin.m`, is based on the Nelder-Mead algorithm as discussed in Section 2.5. Since the built-in optimisation intends to minimise the function, the probability was multiplied with -1 such that the minimum found is truly the maximum. After initial analysis, the maximum was found at negative κ-values, as previously stated that is illogical and impractical. Further research on various adaptations of the built-in function lead to finding the `femsearchminbnd.m` adaptation by D'Errico (2021). This was used to limit the search area to only positive κ-values. Further, the algorithm was set to only iterate a thousand times and to stop if the points of the simplex are within 0.009 of each other. The starting simplex of the Nelder-Mead optimisation was chosen to be the κ-values from the Eurocode.

Chapter 4

Results

The results of the MCMC analysis as well as the MAP optimisation is visualised in the section below.

4.1 Continuous output

To assess the progress of the MCMC analysis while iterating, graphs similar to those in Figure 4.1 were continuously generated. In Figure 4.1, the output of 2 000 iterations were extracted to allow sufficient detail to be visible. Figure 4.1a was important to keep track of the number of different samples assessed until an acceptable sample was found. If a large number of samples were consistently needed, it could indicate that a bad starting point was chosen or that there is an error within the posterior distribution calculation. The connection between Figures 4.1b and 4.1c can be seen in that when there is a dip in the difference between $\pi^*(x)$ and $\pi^*(x_{\text{ref}})$, there is a peak in the acceptance ratio. When the graph in Figure 4.1b is at 0, the sampled values are the same as the Eurocode reference values. When this graph is below 0, the values sampled for that iteration produced a less likely result than the reference values. This influenced the burn-in period chosen to ensure that all the samples considered were more accurate than the Eurocode values. As the probability function used is not normalised, it can produce posterior probabilities larger than 1; therefore, the difference between two posterior probabilities can be larger than 1. This also means that the higher the difference between $\pi^*(x)$ and $\pi^*(x_{\text{ref}})$, the more accurate the x value is.

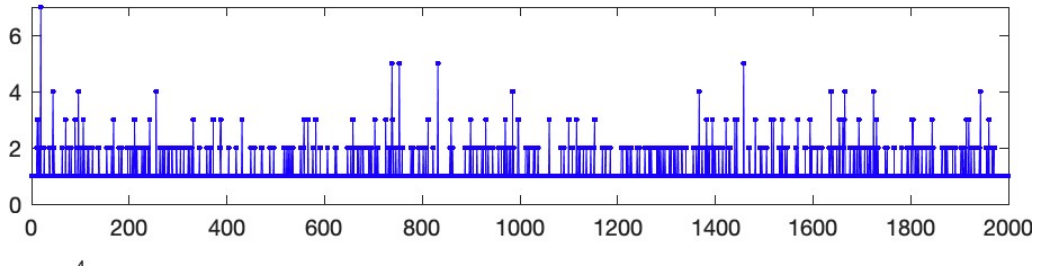

(a) Number of samples drawn before an acceptable sample was found per iteration

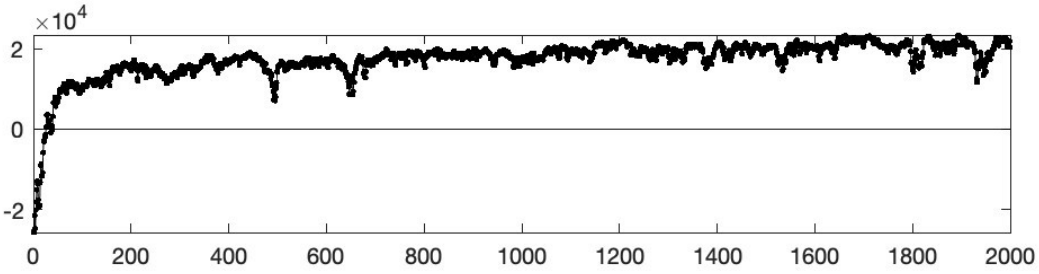

(b) Difference between the accepted x posterior and the reference posterior for each iteration

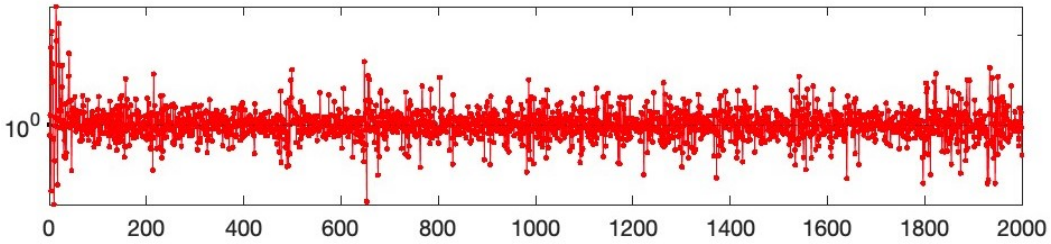

(c) Value of acceptance ratio at each iteration

Figure 4.1: Graphs from continuous output

4.2 Resulting κ-values

The thermal conductivity (κ-values) at key temperatures integral to this project are shown in Table 4.1. As can be seen in Figure 4.2, there was a drastic difference in the thermal diffusivity at 1 200 °C and between 0°C and 200°C. The large difference at 1 200°C can be explained by how the model was created; at that temperature, the majority of the heat is transferred through thermal radiation. The model did not separately model thermal radiation, but instead incorporated the radiation into an equivalent conduction. Between 0°C and 200°C, the modelling of the evaporation was moderately successful as a spike can be seen at 100 °C.

Table 4.1: Posterior thermal conductivity in W/(m K)

°C	EURO	MAP	MCMC
0	0.12	0.062	0.12
60	0.12	0.189	0.278
100	0.12	0.204	0.247
140	0.12	0.096	0.242
200	0.15	0.236	0.243
350	0.07	0.117	0.096
500	0.09	0.039	0.120
800	0.35	0.265	0.234
1200	1.5	7.943	7.467

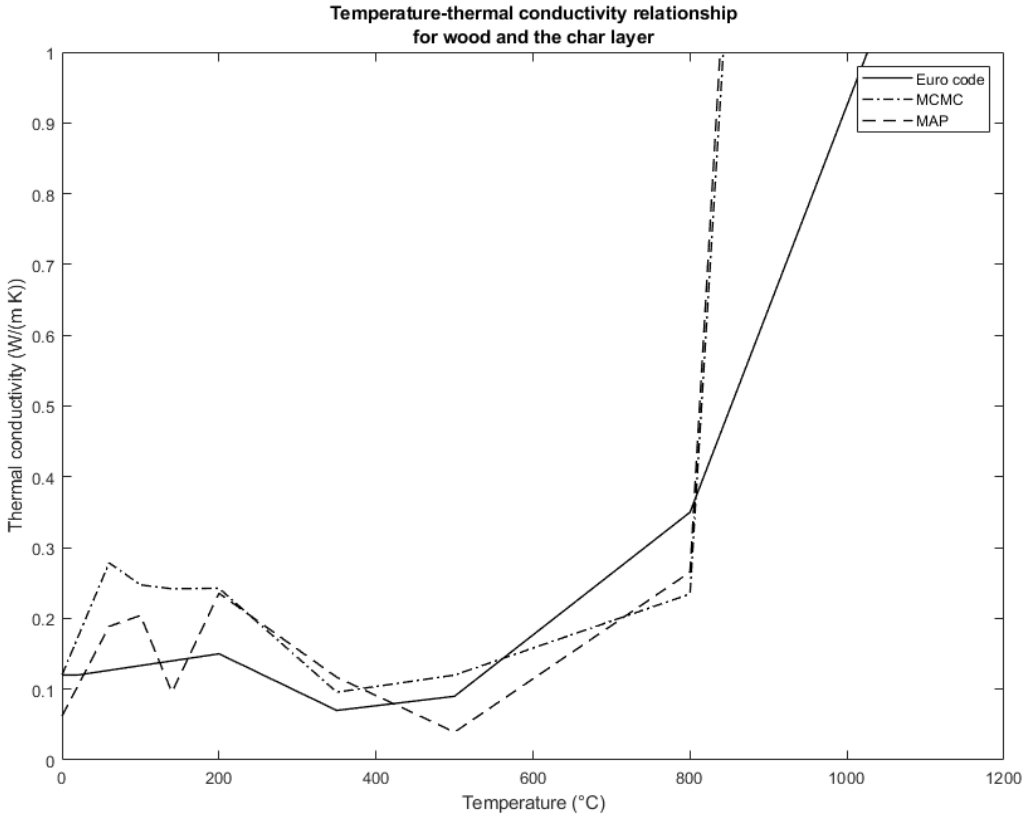

Figure 4.2: Resulting κ-values compared to Eurocode standard values

The uncertainty associated with the κ-values is indicated in Figure 4.3. Error bars indicating one standard deviation have been added.

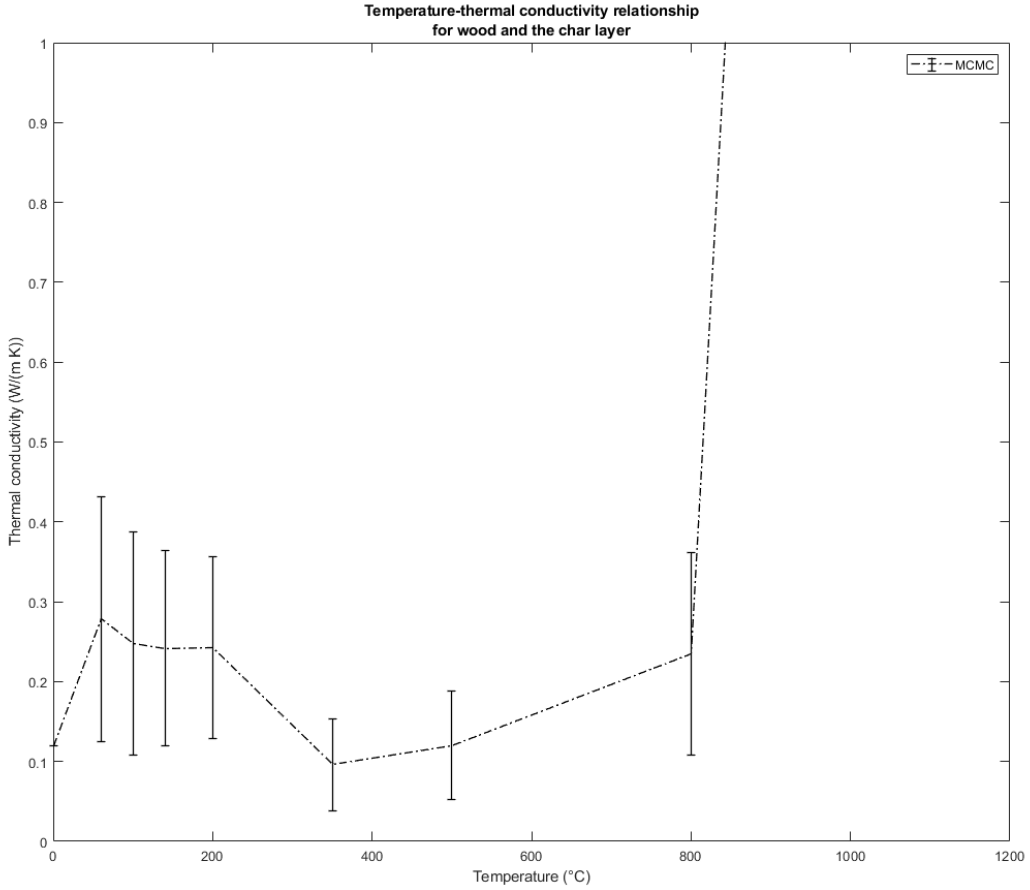

Figure 4.3: Markov chain Monte Carlo κ-values with standard deviation error bars

For each temperature, there will be a different distribution of samples. In Figure 4.5, the distribution of all the samples were plotted in a scatter plot. The resulting κ-values from the MCMC algorithm is plotted in red and the maximum a posteriori is plotted in blue. The asymmetrical distribution is clear in the data as the maximum a posteriori is not in the centre of each distribution.

From the difference between the histogram maximum and the maximum found by the Nelder-Mead optimisation at 140°C (Figure 4.4), it is clear that many more iterations of the MCMC algorithm is needed. In contrast, at 60°C the maximum of the histogram and the MAP is the same, indicating that the distribution at that specific temperature was sufficiently explored. An estimated 500 000 iterations would be needed. As the current iterations already took four days, an additional 14 weeks would have been needed to generate the necessary additional samples. This would have been impractical to achieve during a single semester, as these iterations needed the full computational

capacity of the available machine and prevented any other usage thereof.

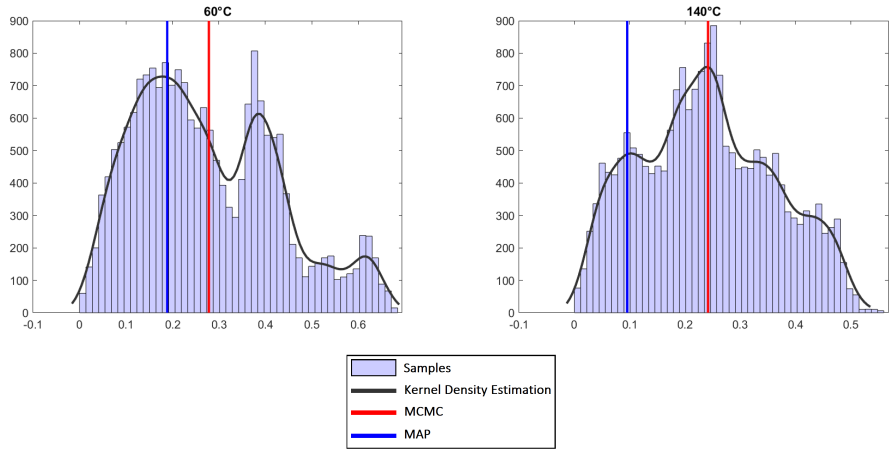

Figure 4.4: Distribution of samples at 60°C and 140°C with MCMC and MAP results indicated

4.2.1 Evaluation of error

Despite the uncertainties connected to the problem, a quantifiable measure of error is still required to allow unbiased assessment of the success of the algorithm and results. The obtained κ-values will be used to rerun the model and obtain the new modelled temperature for each depth. For each depth, the error will be quantified using the norm of the relative error at the seven different depths, denoted as i. The relative error percentages will be calculated according to Equation 4.1. The new modelled output errors are compared to the Eurocode κ-value output errors to assess if the methods used produced a more accurate representation of the data. The error at different depths are summarised in Table 4.2 and the lowest error at that depth is highlighted in green. At a depth of 0 mm, none of the errors are highlighted, as this temperature is independent of the κ-values. This error measurement can be used to asses the error in the model or assumptions made to obtain the model. It is important to note that this error does not only quantify the error in the thermal conductivity, but that any errors due to model assumptions are also encompassed.

$$\epsilon_i = \frac{\|\hat{x}_i - x_i\|_2}{\|x_i\|_2} \times 100 \qquad i = 1, ..., 7 \tag{4.1}$$

Table 4.2: Summary of error percentage between models and data

Depth(mm)	EURO	MAP	MCMC
0	23.11	23.11	23.11
16.5	17.94	14.27	15.35
33	33.40	17.89	18.94
49.5	60.78	37.69	36.93
66	55.18	38.39	30.92
82.5	48.99	34.76	36.60
99	18.18	18.16	18.12
RMSE	40.43	28.01	27.04

The root mean square error (RMSE) for each method was also calculated. There is a definite improvement in the accuracy of the model using the values obtained from the MCMC analysis compared to using the Eurocode values.

4.2.2 Thermal diffusivity

The main intent of this project was to determine the thermal diffusivity of SA-Pine. In Table 4.3, the resulting thermal diffusivity is shown. The thermal diffusivity was calculated using the information in Table 2.1 and Equation 2.6.

Table 4.3: Resulting thermal diffusivity ($\alpha \times 10^{-4}$) in m/s^2

Temp °C	EURO	MAP	MCMC
0	1.64	0.85	1.64
60	1.64	2.58	3.79
100	1.64	2.78	3.37
140	1.64	1.31	3.30
200	2.05	3.21	3.32
350	0.96	1.60	1.31
500	1.23	0.53	1.64
800	4.78	3.62	3.19
1200	25.00	108.00	102.00

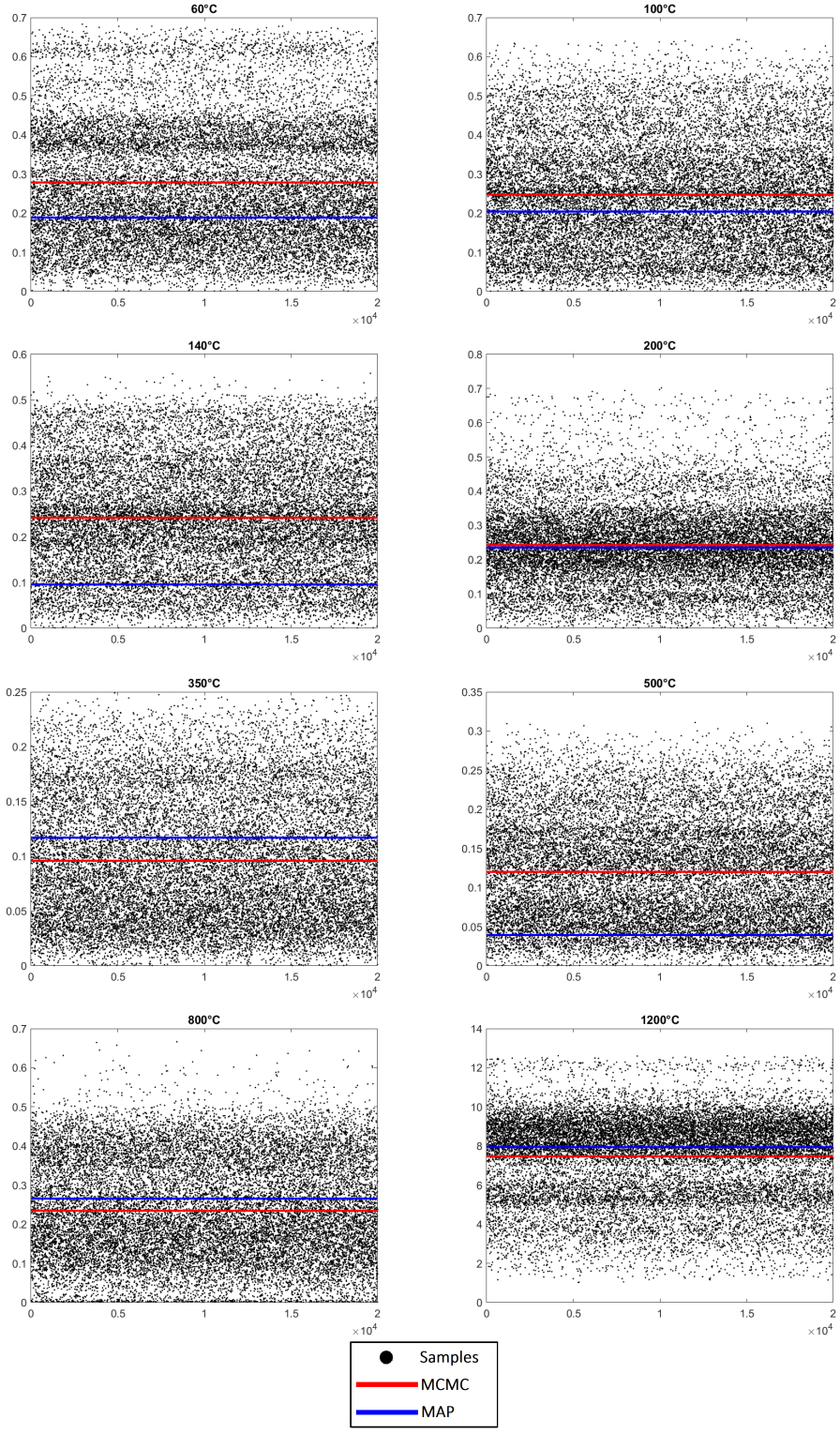

Figure 4.5: Distribution of samples at different temperatures with MCMC and MAP results indicated

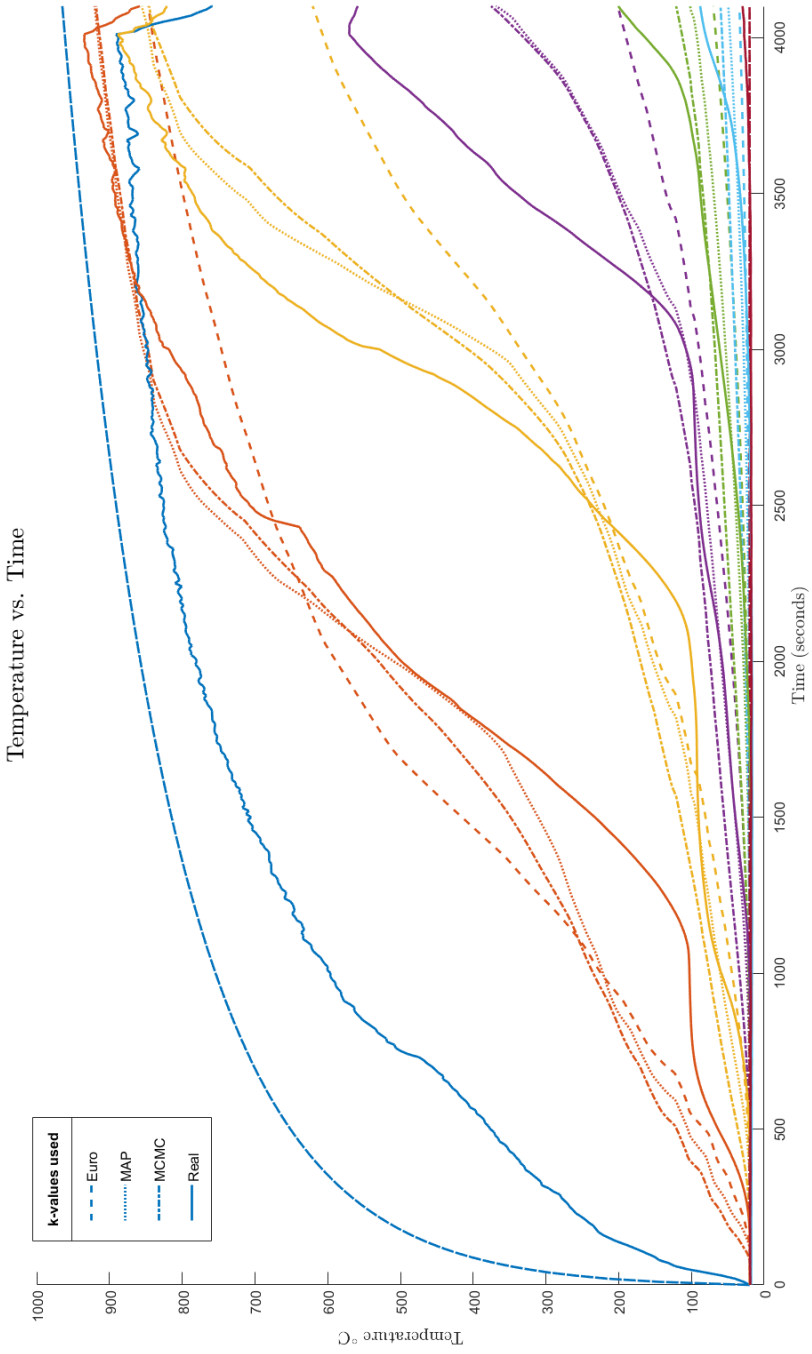

Figure 4.6: Graph of measured data compared to model output

Chapter 5

Discussion

In Figure 4.6, the difference in output from running the model with the new κ-values, Eurocode κ and the measured data can be seen. The attempt at modelling the water evaporation at 100°C was not as successful as initially hoped as the model did not have the same flattening at 100°C as the measured data. The improved accuracy is clear in Table 4.2, as the RMSE for the model using MCMC values is smaller than the error incurred by the same model using the Eurocode thermal conductivity values. There are instances where the error from the model using the MAP κ-values is smaller than the model using the MCMC κ-values; this should not discredit the usage and value of the Markov chain Monte Carlo algorithm as the increased accuracy from the MAP values is only marginal. It is also important to remember that the MCMC algorithm did not necessarily find the population mean due to insufficient iterations. This problem can be simply solved by running more iterations. The error at 49.5mm is visible in Figure 4.6 after 3 000 seconds, where the measured temperature is significantly higher than the Eurocode model output. The increase of error in the centre of the sample is due to the assumption that the timber stays intact. This assumption oversimplifies the problem; as the timber starts charring, pieces of the timber fall off, exposing an internal thermocouple directly to the fire.

The κ-values obtained from the MAP and MCMC analysis give a more accurate model output than those from the Eurocode. This increased accuracy serves as a proof of concept that MCMC analysis can be used to determine more accurate fire ratings and specifically fire resistance.

Fire resistance is measured in minutes, indicating the amount of time from the start of the fire until specific conditions are met. The main conditions taken into account are accounted for by the REI marker system (CETRIS, 2021). In this acronym, 'R' indicates the load-bearing capacity of the structural element and its associated time indicates when the element can no longer carry the design load. 'E' refers to the integrity of the element and the time indicates how long after ignition the fire penetrates the element. 'I' indicates insulation

ability; a limit is set to the temperature of the non-heated side and the time corresponding with that rating refers to when that temperature is exceeded on the non-heated side.

With further development of analytical determination of thermal conductivity and applied finite element models, the data obtained from fire test could be used in a model to determine the REI markers of differently sized elements.

The accuracy of the Markov chain Monte Carlo analysis can be increased by modelling the standard deviation of both the temperatures and the κ-values as random values and solving for them as well. This would make the analysis more heuristic and decrease the dependence of the results on assumptions made by the researcher. Additionally, the program could have been run for a longer time to ensure more samples. and thereby a more accurate approximation of the population mean. Unfortunately, the main limitation in this project was computational time.

It is known that the probability of the thermal conductivity is not symmetrically distributed and that the mean is a more accurate description of the data than the maximum a posteriori. However, the maximum a posterioiri can be used to evaluate if sufficient samples were generated.

Somasundharam and Reddy (2016) also used the Metropolis-Hastings algorithm with Markov chain Monte Carlo (MH-MCMC) sampling to inversely solve heat transfer equations. They additionally compared the MH-MCMC sampling technique to both the parallel tempering sampling technique and the evolutionary Monte Carlo techniques. They found that the standard MH-MCMC sampling technique is accurate enough when a relatively small standard deviation is used, but that the accuracy drastically decreases with higher standard deviations. This is further proof that also solving for the standard deviation would increase the accuracy of the MH-MCMC analysis. They also found that the parallel tempering and evolutionary Monte Carlo techniques were far more accurate even with higher standard deviations.

The research presented in this report can be expanded and applied to the measured data available for eucalyptus. Applying the same algorithm to different data sets and obtaining accurate modelling from both data sets would be confirmation that the algorithm is accurate enough to be further explored for usage in practice.

Chapter 6

Summary and Conclusion

The usage of Markov chain Monte Carlo integration to solve for the thermal diffusivity of cross-laminated SA Pine was successful. The adaptation of the finite element model derived from the heat conduction and diffusion equation enabled the creation of a posterior distribution. The posterior distribution modelled after Bayes' theory of inversion could be traversed and explored using the Markov chain Monte Carlo and the maximum a posteriori could be found using Nelder-Mead optimisation. The resulting κ and α values produced a more accurate model of temperature over time. There is a lot of potential for further optimisation and fine-tuning of these algorithms and models. With further development, this concept could lead to simplified methods of calculating the fire rating of specifically SA Pine and other timber samples. More accurate and accessible fire ratings will help pave the way to improved fire safety.

Appendix A

Relevant code segments

Below are the relevant code segments taken from the MATLAB code that was used to generate the final samples used for analysis.

Prior function

Determines the probability of x assuming a normal probability over the prior values.

```
function q_val = prior_pdf(x_values,sigmaMU)

 global mu_values
 q_val = -0.5*((x_values - mu_values)*(x_values -
    mu_values)')/(sigmaMU^2);

end
```

Likelihood Function

```
function likelihood_pi = likelihood_func(kinput,sigmaT)

% Global variables: physical constants
global_const;
% Global variables: material properties
global_prop
% Global variables: time integration values
global_time;
% Global variables: mesh geometry
global_mesh;
% Global variables of measured temperatures
```

```
global_measuredtemp;

udepths = model_kinput(kinput);
depths_measured = [depth1;depth2;depth3;depth4;depth5;depth6;depth7];
% Where depths measure is the actual measured temperature data from
    the experiment and udepths is the temperature at the same points
    generated by the model using the new k-values.

tempmat = depths_measured - udepths;
likelihood_pi = tempmat(:)'*tempmat(:)/(-2*sigmaT^2);

end
```

Adapted model function

Model adapted to a function as explained in Section 3.2.3. Based on source code from Prof. N de Koker.

```
function udepths = model_kinput(kinput)

global_time;
global_mesh;
global_const;
global_prop;

kpine = kinput;

% Print current number of elements and current sample k-values
kpine(2,:)
fprintf("%d \n",nels);

% Calculate boundary conditions
[isofc, isofcdot] = isofirecurve(tvec);
%isofc(tvec>1000) = 20; % check cooling effect
%isofcdot(tvec>1000) = 0;
atmtemp = tvec*0 + 20; % Celsius
atmtdot = tvec*0;

% Set up initial conditions
unode(:,1) = xnp*0 + atmtemp(1);
unode(1,1) = isofc(1);
vnode(:,1) = xnp*0 + atmtdot(1);
vnode(1,1) = isofcdot(1);%time derivatives
```

```
% Iterate: calculate temperature profile
for i = 2:length(tvec)
    % Set up Dirichlet
    ddir = zeros(nnp,1);
    vdir = zeros(nnp,1);
    ddir(1) = isofc(i);
    vdir(1) = isofcdot(i);
    ddir(nnp) = atmtemp(i);
    vdir(nnp) = atmtdot(i);

    % Assemble global matrices
    Kmat0 = glomatK(unode(:,i-1), ddir);
    Mmat0 = glomatM(unode(:,i-1), ddir);
    Fvec0 = glovecF(unode(:,i-1), ddir);

    % Account for Dirichlet
    Fdir = Kmat0*ddir + Mmat0*vdir;
    Fvec0 = Fvec0 - Fdir;
    Kmat = Kmat0(2:end-1, 2:end-1);
    Mmat = Mmat0(2:end-1, 2:end-1);
    Fvec = Fvec0(2:end-1);

    % Solve for d and ddot in this step
    [unode(2:end-1,i), vnode(2:end-1,i)] = dvnext(
        unode(2:end-1,i-1), vnode(2:end-1,i-1), Kmat, Mmat, Fvec );
    unode(:,i) = unode(:,i) + ddir;
    vnode(:,i) = vnode(:,i) + vdir;

    clear Kmat0 Kmat Fvec0 Fvec Mmat0 Mmat;

end
% Isolate nodes at depth of thermocouples
count = [2 7 12 17 22 27 32];

udepth1 = unode(count(1),2:end);
udepth2 = unode(count(2),2:end);
udepth3 = unode(count(3),2:end);
udepth4 = unode(count(4),2:end);
udepth5 = unode(count(5),2:end);
udepth6 = unode(count(6),2:end);
udepth7 = unode(count(7),2:end);

udepths = [udepth1;udepth2;udepth3;udepth4;udepth5;udepth6;udepth7];

end
```

Function to take next step

This function takes the current vector $\mathbf{x}_n$ and generates a new probable $\mathbf{x}_{n+1}$.

```
function xvalue2 = takexsteps(xvalue1)
   global temps mu_values stepsize sigmastepMU sigmastepT

   locsigma = stepsize*mu_values;
   locxvalue = xvalue1;

   lnMu = log(locxvalue.^2 ./ sqrt(locsigma.^2+locxvalue.^2));
   lnSigma = sqrt(log(locsigma.^2./xvalue1.^2 + 1));

   xvalue2 = max(0, lognrnd(lnMu, lnSigma));
   xvalue2(1) = xvalue1(1);

   xvalue2(xvalue2<locsigma/20) =
       (mu_values(xvalue2<locsigma/20)+xvalue2(xvalue2<locsigma/20))/2;

end
```

MCMC main

```
rng(1e7,"twister");
num_of_runs = 5000;
global temps mu_values stepsize
temps = [0,60,100,140, 200,350,500,800,1200];
mu_values = [0.12, 0.12, 0.12, 0.12, 0.15, 0.07, 0.09, 0.35, 1.5];
    %Based on Eurocode values
stepsize = 0.05;
allMUvalues = zeros([num_of_runs,9]);
instantiate_all();

%% Random start values generate
%rand_x = abs(mu_values * 2);
%rand_x = abs(mu_values + rand_in_rangesz(-0.05,0.5,9));
rand_x = abs(mu_values.*(0.5+rand(1,9)*1.5));
rand_x(1:2) = mu_values(1:2);
rand_sigmaT = 15;
rand_sigmaMU = 0.13;

%% MCMC Instantiate
```

```
sigmaT1 = rand_sigmaT;
sigmaMU1 = rand_sigmaMU;
xvalues1 = rand_x;
alpha = 0.2;

posteriorref = posteriori_func(mu_values,sigmaT1,sigmaMU1);

tic
posterior1 = posteriori_func(xvalues1,sigmaT1,sigmaMU1);
toc

i = 1;
j = 0;
%% Itteration MCMC
while i <= num_of_runs
    j = j + 1;
    xvalues2 = takexsteps(xvalues1);

[mu_values; xvalues1; xvalues2]

    %constant sigma
    sigmaMU2 = sigmaMU1;
    sigmaT2 = sigmaT1;

tic
    posterior2 = posteriori_func(xvalues2,sigmaT2,sigmaMU2);
toc
    %%Acceptance probability
    del = exp((posterior2-posterior1)/(abs(posteriorref)/50));
    q = rand;

[i,j, posterior1, posterior2, del, q]
    if (q < del)

        %Add values to stored accepted values
        allMUvalues(i,:) = xvalues2;
        fprintf("\n Accepted %d\n\n",i);

        %Set accepted value as our new stepping stone
        xvalues1 = xvalues2;
        posterior1 = posterior2;
        post(i) = posterior1-posteriorref;
        comp(i) = del;
        count(i) = j;
        i=i+1;
```

```
        j=0;

       figure(11)
       scatter(temps,allMUvalues(i-1,:),'black','filled');

   end
end

%% Averages
allMUvalues;
for i=1:9
    muAverage(i) = mean(allMUvalues(1:length(count),i));
    muStd(i) = std(allMUvalues(1:length(count),i));
end
```

MAP determination

```
global temps stepsize mu_values
temps = [0,60,100,140, 200,350,500,800,1200];
mu_values = [0.12, 0.12, 0.12, 0.12, 0.15, 0.07, 0.09, 0.35, 1.5];
x_values = mu_values;
stepsize = 0.05;
sigmaT1 = 15;
sigmaMU1 = 0.13;
instantiate_all();

fminopts = optimset('fminsearch');
fminopts.TolX = 0.0009;
fminopts.MaxFunEvals = 1000;
fminopts.MaxIter = 1000;
lowBound= [0.000, 0.000, 0.000, 0.000, 0.000, 0.0000, 0.0000, 0.00,
    0.1];
upBound = [0.8, 0.8, 0.8, 0.8, 0.8, 0.8, 0.8, 0.8, 20];

fun = @(x_values) -1*posteriori_func(x_values,sigmaT1,sigmaMU1);
[mu_map,fval] = fminsearchbnd(fun,
    x_values,lowBound,upBound,fminopts);
```

Appendix B

Derivation of Implemented FEM Model

In this appendix, the derivation of the implemented finite element model is explained in detail.

The balance and heat equations are shown in Equation B.1.

$$q_{,x} - f = 0 \ ...(1) \qquad q = -\kappa u_{,x} \ ...(2) \tag{B.1}$$

Integrating Equation B.1 (1) over the length of the element and introducing a weighting function $w(x)$, we obtain B.2, since the derivative of $w(0)$ is known and $q_{,x}$ is unknown. The first term in Equation B.2 is integrated by parts. After the integration by parts and substituting q with Equation B.1 (2), Equation B.3 is created.

$$\int_{x=0}^{L} w q_{,x} dx - \int_{x=0}^{L} w f dx = 0 \tag{B.2}$$

$$\int_{x=0}^{L} w k u_{,x} dx + \int_{x=0}^{L} w f dx - w q|_0^L = 0 \tag{B.3}$$

In Equation B.3 the u and w need to be defined. Assuming $u \approx u^h$ and $w \approx w^h$ and using the basis function (N^A), Equation B.4 is obtained.

$$\begin{aligned} u_e^h &= \sum_B N^B d^B \quad ; \quad w_e^h = \sum_A N^A c^A \\ u_{e,x}^h &= \sum_B N_{,x}^B d^B \quad ; \quad w_{e,x}^h = \sum_A N_{,x}^A c^A \end{aligned} \tag{B.4}$$

Substituting the u and w functions back, we obtain the Galerkin weak form shown in Equation B.5.

$$\begin{aligned} \sum_e \int_{\Omega_e} w^h_{e,x} k u^h_{e,x} dx + \sum_e \int_{\Omega_e} w^h_e f dx - w(L) q_L + w(0) q_0 &= 0 \\ \int_{\Omega_e} \sum_A \sum_B N^A_{,x} c^A k N^B_{,x} d^B dx + \int_{\Omega_e} \sum_A N^A c^A f dx - \sum_{A \in A_N} c^A q^A &= 0 \end{aligned} \tag{B.5}$$

$$\mathbf{c}_e^T \mathbf{K}_e^{AB} \mathbf{d}_e + \mathbf{c}_e^T \mathbf{F}_e^f - \mathbf{c}_e^T \mathbf{F}_e^q \tag{B.6}$$

where

$$\begin{aligned} K_e^{AB} &= \int_{\Omega_e} N^A_{,x} N^B_{,x} k dx \\ F_e^{Af} &= \int_{\Omega_e} N^A_{,x} f dx \\ F_e^{Aq} &= \begin{cases} q(x_N) & \text{for } x \in \Gamma_N \\ 0 & \text{for other} \end{cases} \end{aligned}$$

$$\begin{aligned} q_{\text{adv}} &= \nu \rho_A c_A \Delta T = h \Delta T \\ \text{with} \quad \nu &= \text{velocity [m/s]}, \\ \rho_A &= \text{density of air, and} \\ c_\rho &= \text{heat capacity of air} \end{aligned} \tag{B.7}$$

$$\begin{aligned} q_{\text{rad}} &= \varepsilon \sigma \phi \left(T_f^4 - T_S^4 \right) \\ \text{with} \quad \varepsilon &= \text{emissivity}, \\ \sigma &= \text{Stefan-Boltzmann constant} \\ &= 5.670 \times 10^{-8}\ W/(m^2 K^4), \text{ and} \\ \phi &= \text{view factor} = 1 \end{aligned} \tag{B.8}$$

Given that T_S and T_F are known a new equivalent heat flux value can be calculated as in Equation 3.10.

$$q_{\text{con}}^{\text{equiv}} = \kappa^{\text{equiv}} \frac{\Delta T}{\Delta L} = q_{\text{rad}} + q_{\text{adv}} \tag{B.9}$$

Due to the clear relationship between heat flux and thermal diffusivity the equivalent diffusivity (κ^{equiv}) can be calculated as shown below in Equation 3.11.

$$\begin{aligned} \kappa^{\text{equiv}} &= \frac{[q_{\text{rad}} + q_{\text{adv}}]}{\Delta T} \\ &= \frac{\epsilon \sigma \phi \Delta \left(T^4 \right)}{\Delta T / \Delta L} + h \Delta L \\ &= \frac{\epsilon \sigma \Delta \left(T^4 \right)}{\Delta T} + h \end{aligned} \tag{B.10}$$

The diffusion equation:

$$q_{,x} - f = \frac{\partial Q}{\partial t} = c_\rho \frac{\partial u}{\partial t} \quad ...(1) \qquad q = -\kappa \frac{\partial u}{\partial x} \quad ...(2) \tag{B.11}$$

Substituting Equation B.11(2) into Equation B.11 and taking the derivative as indicated ($q_{,x}$) produces Equation B.12. As previously discussed, heat conduction (α) is heat diffusion (κ) divided by specific heat (c_p).

$$\begin{gathered} \therefore -\kappa \frac{\partial^2 u}{\partial x^2} - f = c_\rho \frac{\partial u}{\partial t} \rightarrow f = 0 : \\ \frac{\partial^2 u}{\partial x^2} = -\frac{c_\rho}{\kappa} \frac{\partial u}{\partial t} \\ \text{or} \\ \frac{\partial u}{\partial t} = -\alpha \frac{\partial^2 u}{\partial x^2} \end{gathered} \tag{B.12}$$

Let $c_p = \lambda$

$$\therefore -\kappa u_{,xx} - \lambda u_{,t} = f \tag{B.13}$$

Then:

$$\int_0^L w q_{,x} \mathrm{d}x - \int_0^L w \lambda u_{,t} \mathrm{d}x - \int_0^L w f \mathrm{d}x = 0 \tag{B.14}$$

Similar to what was done in Equation B.4, a special approximation is made to obtain Equation B.15.

$$u \approx u^h \rightarrow u_e^h = \sum_A N^A d^A \quad ; \quad w_e^h = \sum_A N^A L^A \tag{B.15}$$

$$\rightarrow \sum_e \int_{\Omega^e} w_{e,x}^h \kappa u_{e,x}^h \mathrm{d}x_e + \sum_e \int_{\Omega^e} w_e^h \lambda u_{e,t}^h \mathrm{d}x_e + \sum_e \int_{\Omega^e} w_e^h f \mathrm{d}x_e - \sum_{e \in \epsilon_A} w q_N = 0 \tag{B.16}$$

$$*_1 : \int_{\Omega^e} \sum_A \sum_B N_{,x}^A c^A \kappa N_{,x}^B d^B \mathrm{d}x = \sum_A \sum_B \left[\int N_{,x}^A N_{,x}^B \kappa \mathrm{d}x \right] d^B = \mathbf{c}_e^T \boldsymbol{\kappa}_e \mathbf{d}_e$$

$$*_2 : \int_{\Omega_e} \sum_A \sum_B N^A c^A \lambda N^B \dot{d}^B \mathrm{d}x = \sum \sum c^A \left[\int N^A N^B \lambda \mathrm{d}x \right] d^B = \mathbf{c}_e^T \mathbf{M}_e \dot{\mathbf{d}}_e$$

$$*_3 : \int_{\Omega^e} \sum_A N^A c^A f \mathrm{d}x = \sum c \int_B^A N f \mathrm{d}x = \mathbf{c}_e^T \mathbf{F}_e^B$$

$$*_4 : \sum_{A\in\mathcal{A}} \kappa^A q_N^A = \mathbf{c}_e^T \mathbf{F}_e^q$$

From all the above equations, the below matrix formulation could be assembled:

$$\mathbf{c}^T\mathbf{K}\mathbf{d} + \mathbf{c}^T\mathbf{M}\dot{\mathbf{d}} = \mathbf{c}^T\mathbf{F} \tag{B.17}$$

Set $\mathbf{d}_0$ equal to the known conditions at time 0.

And $\mathbf{v}_0 = \mathbf{0}$

Also set α as a parameter between 0 and 1. Δt is the time step.

Following the v-form time integration in Hughes Chapter 8, page 460, define $\mathbf{d}_{n+1}$ as in Equation B.18.

$$\mathbf{d}_{n+1} = \mathbf{d}_n + (1-\alpha)\Delta\mathbf{v}_n + \alpha\Delta t\mathbf{v}_{n+1} \tag{B.18}$$

$$(\mathbf{M} + \alpha\Delta t\boldsymbol{\kappa})\mathbf{v}_{n+1} = \mathbf{F}_{n+1} - \boldsymbol{\kappa}\tilde{\mathbf{d}}_{n+1} \tag{B.19}$$

If $\mathbf{M}$ and $\boldsymbol{\kappa}$ independent of time and temperature, it is sufficient to say:

$$\mathbf{v}_{n+1} = (\mathbf{M} + \alpha\Delta t\boldsymbol{\kappa})^{-1}(\mathbf{F}_{n+1} - \boldsymbol{\kappa}\tilde{\mathbf{d}}_{n+1}) \tag{B.20}$$

If κ and λ is independent of position:

$$\begin{aligned} K_e^{AB} &= \int_0^\ell N_{,x}^A N_{,x}^B \kappa \mathrm{d}x \\ &= \kappa \int_0^\ell N_{,x}^A N_{,x}^B \mathrm{d}x \\ &= \kappa \int_{-1}^{+1} N_{,\xi}^A N_{,\xi}^B \xi_{,x}^2 \left|J\right| d\xi \\ &= \kappa \frac{2}{\ell} \int_{-1}^{+1} N_{,\xi}^A N_{,\xi}^B \mathrm{d}\xi \\ &= \pm\frac{\kappa}{\ell} = \begin{cases} +\frac{1}{2} & \text{if } A = B \\ -\frac{1}{2} & \text{if } A \neq B \end{cases} \end{aligned} \tag{B.21}$$

$$\therefore \mathbf{K}_e = \frac{\kappa}{\ell}\begin{bmatrix} +1 & -1 \\ -1 & +1 \end{bmatrix} \tag{B.22}$$

$$M_e^{AB} = \int_0^\ell N^A N^B \lambda \mathrm{d}x = \lambda \int_0^\ell N^A N^B \mathrm{d}x = \frac{\lambda\ell}{2}\int_{-1}^{+1} N^A N^B \mathrm{d}x \tag{B.23}$$

$$N^1N^1 = \frac{1}{4}(1-\xi)^2; N^2N^2 = \frac{1}{4}(1+\xi)^2; N^1N^2 = \frac{1}{4}(1-\xi^2) \tag{B.24}$$

$$N^1 = \frac{1-\xi}{2}; N^2 = \frac{1+\xi}{2} \tag{B.25}$$

Then

$$\begin{aligned} \int N^1 N^1 &= \frac{1}{4}\left[\xi + \frac{1}{3}\xi^3\right]_{-1}^{+1} = \frac{2}{3} \\ \int N^2 N^2 &= \frac{1}{4}\left[\xi + \frac{1}{3}\xi^3\right]_{-1}^{+1} = \frac{2}{3} \\ \int N^1 N^2 &= \frac{1}{4}\left[\xi - \frac{1}{3}\xi^3\right]_{-1}^{+1} = \frac{1}{3} \end{aligned} \tag{B.26}$$

$$\therefore \mathbf{M}_e = \frac{\lambda\ell}{6}\begin{bmatrix} 2 & 1 \\ 1 & 2 \end{bmatrix} \tag{B.27}$$

$$\mathbf{F}_e^{fA} = \int_0^\ell N f \mathrm{d}x = f\frac{\ell}{2}\int_{-1}^{+1} N \mathrm{d}x = f\frac{\ell}{2} \therefore \mathbf{F}_e^f = \frac{f\ell}{2}\begin{Bmatrix} 1 \\ 1 \end{Bmatrix} \tag{B.28}$$

More generally, matrix K_e and M_e are:

$$\begin{aligned} K_e^{AB} &= \int_0^\ell N_{,x}^A N_{,x}^B \kappa \mathrm{d}x \text{ with } \kappa = N^1\kappa^1 + N^2\kappa^2 \\ &= \left(\frac{\ell}{2}\right)\left(\frac{\pm 1}{4}\right)\left(\frac{4}{\ell^e}\right)\int_{-1}^{+1}\left[\frac{1-\xi}{2}\kappa^{(1)} + \frac{1+\xi}{2}\kappa^{(2)}\right]\mathrm{d}\xi \end{aligned} \tag{B.29}$$

and

$$M_e^{AB} = \int_0^\ell N^A N^B \lambda \mathrm{d}x \quad \text{with} \quad \lambda = N^1\kappa^{(1)} + N^2\kappa^{(2)} \tag{B.30}$$

If $A = 1$ and $B = 1$, then M_e is calculated as shown below in Equation B.31.

$$\begin{aligned} M_e^{11} &= \left(\frac{\ell}{2}\right)\int_{-1}^{+1}\frac{1}{4}(1-\xi)^2\left[\frac{1-\xi}{2}\cdot\lambda^{(1)} + \frac{1+\xi}{2}\cdot\lambda^{(2)}\right]\mathrm{d}\xi \\ &= \frac{\ell}{16}\int_{-1}^{+1}\left[(1-\xi)^2(1-\xi)\lambda^{(1)} + (1-\xi)^2(1+\xi)\lambda^{(2)}\right]\mathrm{d}\xi \\ &= \frac{\ell}{16}\left[\lambda^{(1)}\int_{-1}^{+1}(1-\xi)^2(1-\xi)\mathrm{d}\xi + \lambda^{(2)}\int_{-1}^{+1}(1-\xi)^2(1+\xi)\mathrm{d}\xi\right] \\ &= \frac{\ell}{16}\left[\lambda^{(1)}\cdot 4 + \lambda^{(2)}\cdot\frac{4}{3}\right] \\ &= \frac{\ell}{4}\left[\lambda^{(1)} + \frac{\lambda^{(2)}}{3}\right] \end{aligned} \tag{B.31}$$

When $A = 2$ and $B = 2$:

$$\begin{aligned} M_e^{22} &= \frac{\ell}{16}\int_{-1}^{+1}\left[(1+\xi)^2(1-\xi)\lambda^{(1)} + (1+\xi)^2(1+\xi)\lambda^{(2)}\right]\mathrm{d}\xi \\ &= \frac{\ell}{4}\left[\frac{\lambda^{(1)}}{3} + \lambda^{(2)}\right] \end{aligned} \tag{B.32}$$

When $A = 1$ and $B = 2$ **or** $A = 2$ and $B = 1$:

$$\begin{aligned} M_e^{12} &= \frac{\ell}{16}\int_{-1}^{+1}\left[(1-\xi^2)(1-\xi)\lambda^{(1)} + (1-\xi^2)(1+\xi)\lambda^{(2)}\right]\mathrm{d}\xi \\ &= \frac{\ell}{4}\left[\frac{\lambda^{(1)}}{3} + \frac{\lambda^{(2)}}{3}\right] \\ &= \frac{\ell}{12}\left[\lambda^{(1)} + \lambda^{(2)}\right] \end{aligned} \tag{B.33}$$

The matrix can then be assembled from the above Equations B.31, B.32, and B.33:

$$\begin{aligned} \mathbf{M}_e &= \frac{\ell}{4}\left(\lambda^{(1)}\begin{bmatrix}1 & \frac{1}{3}\\ \frac{1}{3} & \frac{1}{3}\end{bmatrix} + \lambda^{(2)}\begin{bmatrix}\frac{1}{3} & \frac{1}{3}\\ \frac{1}{3} & 1\end{bmatrix}\right) \\ &= \frac{\ell}{12}\left(\lambda^{(1)}\begin{bmatrix}3 & 1\\ 1 & 1\end{bmatrix} + \lambda^{(2)}\begin{bmatrix}1 & 1\\ 1 & 3\end{bmatrix}\right) \end{aligned} \tag{B.34}$$

The same can be done to assemble the K matrix as shown below.

$$\begin{aligned} K_e^{AB} &= \left(\frac{\pm 1}{2\ell}\right)\int_{-1}^{+1}\left[\frac{1-\xi}{2}\kappa^{(1)} + \frac{1+\xi}{2}\kappa^{(2)}\right]\mathrm{d}\xi \\ &= \left(\frac{\pm 1}{2\ell}\right)\left[\kappa^{(1)} + \kappa^{(2)}\right] \end{aligned} \tag{B.35}$$

$$\mathbf{K}_e = \frac{1}{2\ell}\left(\kappa^{(1)}\begin{bmatrix}1 & -1\\ -1 & 1\end{bmatrix} + \kappa^{(2)}\begin{bmatrix}1 & -1\\ -1 & 1\end{bmatrix}\right) \tag{B.36}$$

Thereafter the $\mathbf{F}_e$ matrix

$$\begin{aligned} F_e^A &= \int_0^{\ell} N^A f\,\mathrm{d}x \\ &= \frac{\ell}{2}\int_{-1}^{+1} N^A f\,\mathrm{d}\xi \end{aligned} \tag{B.37}$$

$$\begin{aligned} F_e^1 &= \frac{\ell}{2}\int_{-1}^{+1}\left(\frac{1-\xi}{2}\right)\cdot\left[\frac{1-\xi}{2}\cdot f^{(1)} + \frac{1+\xi}{2}\cdot f^{(2)}\right] \\ &= \frac{\ell}{8}\int_{-1}^{+1}\left[(1-\xi)^2\cdot f^{(1)} + \left(1-\xi^2\right)\cdot f^{(2)}\right]\mathrm{d}\xi \end{aligned} \tag{B.38}$$

$$F_e^2 = \frac{\ell}{8}\int_{-1}^{+1}\left[(1-\xi^2)\cdot f^{(1)} + (1+\xi)^2\cdot f^{(2)}\right]\mathrm{d}\xi \tag{B.39}$$

$$\begin{aligned}\therefore \mathbf{F}_e &= \frac{\ell}{8}\left(f^{(1)}\begin{Bmatrix}\frac{8}{3}\\ \frac{4}{3}\end{Bmatrix} + f^{(2)}\begin{Bmatrix}\frac{4}{3}\\ \frac{8}{3}\end{Bmatrix}\right) + \sum_{A\in\mathcal{A}_N} q^{(A)}\begin{Bmatrix}-\delta^{A1}\\ +\delta^{A2}\end{Bmatrix}\\ &= \frac{\ell}{6}\left(f^{(1)}\begin{Bmatrix}2\\ 1\end{Bmatrix} + f^{(2)}\begin{Bmatrix}1\\ 2\end{Bmatrix}\right) + \sum_{A\in\mathcal{A}_N} q^{(A)}\begin{Bmatrix}-\delta^{A1}\\ +\delta^{A2}\end{Bmatrix}\end{aligned} \tag{B.40}$$

After assembly but before Dirichlet boundaries are applied:

$$\bar{\mathbf{c}}^T\bar{\mathbf{K}}\bar{\mathbf{d}} + \bar{\mathbf{c}}^T\bar{\mathbf{M}}\dot{\bar{\mathbf{d}}} = \bar{\mathbf{c}}^T\bar{\mathbf{F}} \tag{B.41}$$

When the Dirichlet boundaries below (Equation B.42) are applied to the matrices shown in Equation B.41, they can be simplified to Equation B.43.

$$\begin{aligned} c_1 = 0 \quad &\text{and} \quad c^{np} = 0\\ d_1 = u_{\text{fire(t)}} \quad &\text{and} \quad d^{np} = u_{\text{air}}\end{aligned} \tag{B.42}$$

Then:

$$\begin{aligned}&\mathbf{c}^T\cdot\mathbf{K}\cdot\mathbf{d} + \mathbf{c}^T\cdot\mathbf{M}\cdot\dot{\mathbf{d}} = \mathbf{c}^T\cdot\mathbf{F}' - \mathbf{c}^T\\ &(\{K'\}d' + \{K^{np}\}d^{np}) - \mathbf{c}^T\left(\{M'\}\dot{d}' + \{M^{np}\}\dot{d}^{np}\right)\end{aligned} \tag{B.43}$$

And so:

$$\mathbf{K}\cdot\mathbf{d} + \mathbf{M}\cdot\dot{\mathbf{d}} = \mathbf{F}' - \mathbf{F}^{Ke} - \mathbf{F}^{Me} = \mathbf{F} \tag{B.44}$$

Solve as

$$\begin{aligned}\tilde{\mathbf{d}}_{n+1} &= \mathbf{d}_n + (1-\alpha)\Delta t\mathbf{v}_n\\ (\mathbf{M}+\alpha\Delta t\mathbf{K})\mathbf{v}_{n+1} &= \mathbf{F}_{n+1} - \mathbf{K}\tilde{\mathbf{d}}_{n+1}\\ \rightarrow \mathbf{v}_{n+1} &= (\mathbf{M}+\alpha\Delta t\mathbf{K})^{-1}(\mathbf{F}_{n+1} - \mathbf{K}\tilde{\mathbf{d}}_{n+1})\\ \rightarrow \mathbf{d}_{n+1} &= \tilde{\mathbf{d}}_{n+1} + \alpha\Delta t\mathbf{v}_{n+1}\\ \mathbf{v} &= \dot{\mathbf{d}}\end{aligned} \tag{B.45}$$

List of References

Brownlee, J. (2019 Nov [Online]). A Gentle Introduction to Markov chain Monte Carlo for Probability. Machine Learning Mastery, Blog.
Available at: https://machinelearningmastery.com/markov-chain-monte-carlo-for-probability/

CEN (2004). *BS EN 1995-1-2:2004. Eurocode 5: Design of timber structures - General - Structural fire design.* BSI, London.

CETRIS (2021). Application of CETRIS boards in fire protection pursuant to EN-standards. Information booklet. Obtained from www.cetris.cz.

Cheng, A. and Cheng, D. (2005 03). Heritage and early history of the boundary element method. *Engineering Analysis with Boundary Elements*, vol. 29, pp. 268–302.

Cook, J.D. (2016 Jan [Online]). MCMC burn-in. John D. Cook Consulting.
Available at: https://www.johndcook.com/blog/2016/01/25/mcmc-burn-in/comment-page-1/?unapproved=1094214&moderation-hash=912d585bd365341b032df1d4f1bddf3b#comment-1094214

Courant, R. (1943). Variational methods for the solution of problems of equilibrium and vibrations. *Bulletin of the American Mathematical Society*, pp. 1–23. ISSN 1088-9485.
Available at: https://doi.org/10.1090/S0002-9904-1943-07818-4

D'Errico, J. (2021). fminsearchbnd, fminsearchcon. MATLAB Central File Exchange.
Available at: https://www.mathworks.com/matlabcentral/fileexchange/8277-fminsearchbnd-fminsearchcon

Fish, J.J. (2007). *A first course in finite elements*. John Wiley, Chichester. ISBN 9780470035801.

Fourier, J. (1878). *The analytical theory of heat.* Cambridge University Press.

Frayssinhes, R., Girardon, S., Marcon, B., Denaud, L. and Collet, R. (2020). A simple method to determine the diffusivity of green wood. *BioRes*, vol. 3, no. 15, pp. 6539–6549.

Gilks, W.R., Richarson, S. and Spiegelhalter, D.J. (1996). *Markov chain Monte Carlo in practice*. London, 1st edn.

Gupta, K. and Meek, J. (1996). A brief history of the beginning of the finite element method. *International Journal for Numerical Methods in Engineering*, vol. 39, pp. 3761–3774.

Hughes, T. (1987). *The Finite Element Method: Linear Statistic and dynamic finite element analysis*. Englewood Cliffs, New Jersey.

ISO (1999). *ISO 834 Fire-resistance test - Elements of building construction*. International Organization for Standardization, Geneva.

Joglekar, S. (2016 Jan). Nelder-Mead optimization. Sachin Joglekar's Blog. Available at: `https://codesachin.wordpress.com/2016/01/16/nelder-mead-optimization/`

Kaipio, J. and Somersalo, E. (2005). *Statistical and Computational Inverse Problems*. Verlag New York.

König, J. and Walleij, L. (1999). *One-dimensional Charring of timber exposed to standard and parametric fires in initially unprotected and postprotection situations*. Institutet för träteknisk forskning, Stockholm.

Lagarias, J., Reeds, J., Wright, M. and Wright, P. (1998 Dec). Convergence properties of the Nelder–Mead simplex method in low dimensions. *SIAM Journal on Optimization*, vol. 9, pp. 112–147.

MATLAB (2021). fminsearch.html. Online documentation. Available at: `https://ch.mathworks.com/help/matlab/ref/fminsearch.html`

Meyn, S. and Tweedie, R. (1993 Jan). *Markov Chains and Stochastic Stability*, vol. 92. Springer Verlag.

Murphy, K.P. (2012). *Machine learning : A Probabilistic Perspective*. The MIT Press, Cambridge, Massachusetts. ISBN 9780262018029.

Robert, C.P. and Casella, G. (2004). *Monte Carlo Statistical Methods*, vol. 42. 2nd edn. Springer New York. ISBN 9781441919397.

Salvadori, V. (2017 12). *The Development of a Tall Wood Building*. Master's thesis, Polytechnic University of Milan and TU Wien.

Shi, L. and Chew, M.Y.L. (2021 Aug). A review of thermal properties of timber and char at elevated temperatures. *Indoor and Built Environment*, pp. 1–16. `https://doi.org/10.1177/1420326X211035557`. Available at: `https://doi.org/10.1177/1420326X211035557`

Somasundharam, S. and Reddy, K. (2016 Feb). Inverse estimation of thermal properties using Bayesian inference and three different sampling techniques. *Inverse Problems in Science and Engineering*.

Thi, V., Khelifa, M., Ganaoui, M.E. and Rogaume, Y. (2016 Aug). Modelling of heat transfer in timber exposed to fire. In: *World conference on timber engineering*.

van der Westhuyzen, S., Walls, R. and de Koker, N. (2020). Fire tests of South African cross-laminated timber wall panels: Fire ratings, charring rates, and delamination. *Journal of the South African Institution of Civil Engineering*, vol. 62, no. 1, pp. 33–41. ISSN 23098775.

Wagner, P.-R., Marelli, S. and Sudret, B. (2021). Bayesian model inversion using stochastic spectral embedding. *Journal of Computational Physics*, vol. 436, p. 110141. ISSN 0021-9991.
Available at: `https://www.sciencedirect.com/science/article/pii/S0021999121000334`

White, R. and Dietenberger, M. (2001). Wood products: Thermal degradation and fire. In: Buschow, K.H.J., Cahn, R.W., Flemings, M.C., Ilschner, B., Kramer, E.J., Mahajan, S. and Veyssière, P. (eds.), *Encyclopedia of Materials: Science and Technology*, pp. 9712–9716. Elsevier, Oxford. ISBN 978-0-08-043152-9.
Available at: `https://www.sciencedirect.com/science/article/pii/B0080431526017630`

Wiecki, T. (2015 Nov [Online]). MCMC sampling for dummies. While My MCMC Gently Samples, Blog.
Available at: `https://twiecki.io/blog/2015/11/10/mcmc-sampling/`

Zienkiewicz, O. and Taylor, R. (2000). *The Finite Element Method*, vol. Volume 1: The Basis. 5th edn. Butterworth-Heinemann. ISBN 0 7506 5049 4.